Materials Advances

ROYAL SOCIETY OF CHEMISTRY

PAPER

View Article Online
View Journal

Cite this: DOI: 10.1039/d6ma00114a

Enhanced anticorrosion performance of antipyrine derivatives on mild steel in an acidic environment: an experimental and theoretical analysis

Adil Afaq,[ab] Muhammad Aamir, *[a] Shahid Aziz,*[a] Simon Woodward, [b] Muhammad Haroon,[c] Zaroon Sajid, [a] Md. Akhtaruzzaman,*[d] Md. Shahiduzzaman,[e] Qamar Wali,[fg] Jean-Michel Nunzi *[eh] and It Ee Lee*[fg]

Efficient and structurally diverse organic corrosion inhibitors remain a major challenge for mild steel protection in acidic environments. In this study, three novel adamantyl amide derivatives of 4-aminoantipyrine, **M1**, **M2**, and **M3**, were synthesized and evaluated to investigate the influence of steric effects and accessibility of donor sites on corrosion inhibition performance. The corrosion inhibition performance was examined by weight loss measurements, potentiodynamic polarization (PDP), electrochemical impedance spectroscopy (EIS), and surface characterization techniques, such as SEM, EDX, FESEM, and XPS, along with density functional theory (DFT) calculations. Among the investigated compounds, **M1** exhibited superior inhibition efficiency, achieving up to 98.92% at 0.5 mM in 1.0 M HCl, outperforming its sterically hindered analogs **M2** and **M3**. The inhibition efficiency increased with concentration and immersion time but decreased with temperature, indicating a predominantly physisorption-driven process. The thermodynamic parameters ($E_a \approx 44–55$ kJ mol^{-1}; $\Delta G \approx -10$ to -16 kJ mol^{-1}) further support a mixed adsorption mechanism with dominant electrostatic interactions. The electrochemical results revealed a significant reduction in the corrosion current density and enhanced polarization resistance, confirming the formation of a protective inhibitor film. Surface analyses demonstrated the formation of a compact and adherent layer, particularly for **M1**, which correlated with its superior performance. DFT analysis enabled molecular-level understanding of the process, which showed that adsorption was favored by low energy gaps, high softness values, and high electron transfer ability. Compared to conventional antipyrine-based Schiff bases, the presence of an adamantyl amide moiety offers dual functionality for surface shielding and steric modulation for electron donation. The present investigation has established the importance of steric effects around the adsorption active sites for the effective design of high-performance organic inhibitors for corrosion protection.

Received 23rd January 2026,
Accepted 7th April 2026

DOI: 10.1039/d6ma00114a

rsc.li/materials-advances

1. Introduction

The problem of mild steel corrosion in acidic environments has been a major challenge in many industrial processes, such as pickling, descaling, and oil well acidizing, where hydrochloric acid is commonly used as an aggressive medium. Material degradation becomes very fast under such conditions, causing operational inefficiencies and huge economic losses globally.[1–3] Organic corrosion inhibitors are one of the most effective and practical anticorrosion methods among various corrosion mitigation strategies. This is mainly because these inhibitors work by adsorbing onto metal surfaces and forming protective films that inhibit electrochemical reactions.[4–6] The molecular structure of these compounds, especially the presence of heteroatoms (N, O, S), π-electron systems, and functional groups that can facilitate adsorption and surface interaction, greatly

[a] Department of Chemistry, Mirpur University of Science and Technology (MUST), Mirpur-10250, AJK, Pakistan. E-mail: amir.chem@must.edu.pk, aamirorg@gmail.com, drshahid.chem@must.edu.pk
[b] GSK, Carbon Neutral Laboratories for Sustainable Chemistry, University of Nottingham, Jubilee Campus, 6 Triumph Rd, Lenton, Nottingham NG7 2GT, UK
[c] Department of Chemistry and Biochemistry, Miami University, 651 E. High Street, Oxford, Ohio 45056, USA
[d] Department of Chemical Engineering, Faculty of Engineering, Islamic University of Madinah, 42351 Madinah, Saudi Arabia. E-mail: makhtar@iu.edu.sa
[e] Nanomaterials Research Institute, Kanazawa University, Kakuma, Kanazawa 920-1192, Japan
[f] Faculty of Artificial Intelligence and Engineering, Multimedia University, 63100 Cyberjaya, Malaysia. E-mail: ielee@mmu.edu.my
[g] Centre for Smart Systems and Automation, COE for Robotics and Sensing Technologies, Multimedia University, 63100 Cyberjaya, Selangor, Malaysia
[h] Department of Physics, Engineering Physics and Astronomy, Queen's University, Kingston, Ontario K7L-3N6, Canada. E-mail: nunzijm@queensu.ca

determines their inhibition efficiency.[7–9] 4-Aminoantipyrine derivatives have emerged as corrosion inhibitors because of their structural flexibility, easy functionalization, and multiple adsorptive active sites.[10–12] Recent studies have revealed that 4-aminoantipyrine based Schiff bases have good inhibition power, mainly because their electron-donating capacity and conjugation effect are boosted, thereby favoring metal surface adsorption.[13–16] Although many 4-aminoantipyrine-based inhibitors have been described, previous studies were based on the Schiff base series, for which the optimization of the inhibitory properties was achieved mainly through aromatic substitution and alteration of electron density.[12,17–19]

More importantly, previous research does not provide a thorough understanding of the role steric hindrance around adsorption-active centers plays in inhibitor performance. The addition of bulky groups can produce a hydrophobic surface and better barrier properties; however, very crowded conditions with large groups may physically block the key atoms (N and O) from reaching the metal surface, thereby decreasing the adsorption strength.[20,21] The balance between hydrophobic improvement and steric restriction, which is largely unexplored, is an important deficiency in the scientific design of effective corrosion inhibitors.[22–24]

The adamantyl amide-functionalized 4-aminoantipyrine derivatives could provide the solution to these issues. The adamantyl moiety, which has a unique cage-like skeleton and is very hydrophobic, is anticipated to improve surface coverage and lead to the formation of a dense and stable protective layer.[25,26] Meanwhile, its addition through amide bonds results in a well-structured means to systematically assess the effect of steric hindrance on adsorption efficiency.[27] Unlike classic antipyrine or Schiff base inhibitors, this concept allows for a direct comparison of molecules with different steric environments surrounding the adsorption-active sites.[28] Therefore, hydrophobic surface coverage to steric accessibility of electron-donating centers determines the corrosion inhibition performance. More precisely, it is proposed that limiting steric hindrance around N and O atoms results in stronger adsorption and higher inhibition efficiency, while greater steric congestion prevents effective interaction with the metal surface; however, the electronic properties are favorable.[29,30]

Herein, three adamantyl derivatives of 4-aminoantipyrine inhibitors (**M1**, **M2** and **M3**) were synthesized, and their performance was assessed through weight loss determination, potentiodynamic polarization (PDP), and electrochemical impedance spectroscopy (EIS). Using surface characterization methods (SEM, EDX, FESEM, and XPS), adsorption and protective film formation were validated, and molecular-level insights into electronic structure and reactivity were revealed through density functional theory (DFT) computations.[31–33] In the present study, for the first time, the application of adamantane amide functionalization as an alternative approach for the optimization of antipyrine-based inhibitors was demonstrated, which allows for the optimization of not only the inhibitory properties but also the mechanistic investigation of the effects of steric hindrance on electron donation and adsorption ability. Compared with the previously investigated antipyrine-based inhibitors, the new compounds provide a better understanding of the structure–property relationships by allowing for the investigation of the effects of the distance and steric hindrance between the electron-donating sites and the hydrophobic cage unit. In this regard, **M1** exhibited superior performance because the donor centers were less sterically hindered, allowing stronger interactions with the mild steel surface and more effective protective film formation.

2. Experimental section

2.1. Materials and methods

The entire chemical used in the synthesis of organic inhibitors (**M1**, **M2** and **M3**) were of analytical grade and used as received without any further purification. These chemicals were purchased from Sigma-Aldrich, Merck, Fischer Chemicals and Acros Organics. The progress of chemical reactions and purity of synthesized products was checked by thin layer chromatography (TLC) aluminum sheets coated with Kiesel gel 60, F_{254} (Merck). The melting points were measured by open capillary tubes in DMP-300 A&E lab, UK. The functional groups were identifying through IR spectra recorded on Bruker Alpha 4 using attenuated total reflectance (ATR) on platinum. The proton (^{1}H-NMR), carbon-13 (^{13}C-NMR), and correlated nuclear magnetic resonance spectroscopy (COSY), heteronuclear single quantum coherence spectroscopy (HSQC) measurements were performed on Bruker Ascend™ 400 and Bruker Ascend™ 500 MHz spectrometer. The mass spectra were recorded on the Agilent Technologies mass spectrometer micro time of flight electrospray ionization (TOF-ESI) positive and negative targeted modes. The tafel, bode, phase angle and nyquist plots were recorded on the Gamray Potentiostat.

2.2. Synthesis

2.2.1. 4-Amino-1,5-dimethyl-2-phenyl-1*H*-pyrazol-3(2*H*)-one (2). The ester derivative of 4-aminoantipyrine (**1**) (12.5 mmol) was dissolved in dichloromethane DCM (6.25 mL) and 98% sulfuric acid (6.25 mmol) under stirring for 6 h. The progress of the formation of 4-aminoantipyrine (**2**) was continuously checked by TLC. Upon cessation of product production, extraction of (**2**) was conducted using 2.0 M sodium hydroxide (4.5 mL) in combination with an aqueous phase rendered acidic through the addition of 37% HCl (20 mL), followed by extraction with diethyl ether (4.5 mL). The organic phase was then washed with 10% aqueous Na_2SO_4 and dried with anhydrous Na_2SO_4 to obtain a pure product.[34] Yield 98%, melting point 106–110 °C, ^{1}H-NMR Bruker 400 MHz (DMSO-d_6, ppm): [s, 3H, CH_3], 2.09 [s, 3H, N–CH_3], 2.73 [s, 2H, NH_2], 3.84 [m, 1H, Ar-H], 7.23 [m, 4H, Ar-H], 7.44. ^{13}C-NMR (DMSO-d_6, ppm) [10.38, 38.79, 120.58, 122.31, 125.58, 129.39, 135.95, 136.09, 161.89], HRMS (Bruker Micro TOF) *m/z* [M + H, 204.11, M + Na, 226.09].

2.2.2. 4-((1,5-Dimethyl-3-oxo-2-phenyl-2,3-dihydro-1*H*-pyrazol-4-yl)amino)-4-oxobutanoic acid (4). 4-Aminoantipyrine (1 mmol) (**2**) solution in ethyl acetate was added dropwise to a stirred

solution of succinic anhydride (**3**) (1 mmol) in ethyl acetate (20.0 mL) in an ice bath and under a N_2 purge environment. The reaction mixture was stirred for 8.0 hours at room temperature after 30 min. The light yellow colored precipitates separated from the solvent through vacuum filtration and recrystallized the product (**4**) in chloroform.[35] Yield 98.6%, melting point 199–202 °C, IR cm^{-1}: [3283 (NH amide), 2929 (OH of carboxylic acid), 1741 (C═O), 1666 (C═O), 1615 (C═C) and 1600 (C═O)], ^{1}H-NMR Bruker 400 MHz (DMSO-d_6, ppm): [s, 3H, CH_3], 2.09 [m, 4H, CH_2–CH_2], 2.51 [s, 3H, N–CH_3], 3.03 [m, 3H, Ar-H], 7.30 [m, 2H, Ar-H], 7.50 [s, 1H, NH] 9.11, [s, 1H, COOH] 12.10. ^{13}C-NMR (DMSO-d_6, ppm) [11.65, 29.54, 30.34, 36.54, 108.16, 123.86, 126.61, 129.54, 135.56, 152.89, 162.31, 171.09, 174.26], HRMS (Bruker Micro TOF) *m/z* [M + H, 304.12, M + Na, 326.11, M − H, 302.11].

2.2.3. Synthesis of *N*1-(adamantan-1-yl)-*N*4-(1,5-dimethyl-3-oxo-2-phenyl-2,3-dihydro-1*H*-pyrazol-4-yl)succinamide (M1). *N*1-((*S*)-1-((3*S*,5*S*,7*S*)-Adamantan-1-yl)ethyl)-*N*4-(1,5-dimethyl-3-oxo-2-phenyl-2,3-dihydro-1*H*-pyrazol-4-yl)succinamide (**M2**), *N*1-(1,5-dimethyl-3-oxo-2-phenyl-2,3-dihydro-1*H*-pyrazol-4-yl)-N4-((2*S*,4*R*)-1,7,7-acid) (**4**) (1 eq.) was added to a solution of amines (0.1 mol), DMAP (0.1 eq.), and EDCl (4 eq.) in DCM (20 mL) under stirring at room temperature and an inert (N_2 purge) environment. The resulting mixture was stirred at room temperature for 48 h. Subsequently, the product was extracted with water and saturated with aqueous sodium hydrogen carbonate. The organic layer was concentrated using a rotary evaporator, and the product was separated on a silica column using a suitable solvent system. The NMR spectra of products (**M1–M3**) were recorded in deuterated DMSO-d_6.[36]

*2.2.3.1. (**M1**).* *N*1-(Adamantan-1-yl)-*N*4-(1,5-dimethyl-3-oxo-2-phenyl-2,3-dihydro-1*H*-pyrazol-4-yl)succinamide. Yield 96%, melting point 229–232 °C, solubility DMSO/DMF, IR cm^{-1}: [3358 N–H, 2904 N–H, 2848 C–H aromatic, 1643 C═O], ^{1}H-NMR Bruker 400 MHz (DMSO-d_6, ppm): [m, 6H, 3CH_2], 1.60 [m, 6H, 3CH_2], 1.92 [m, 3H, 3CH] 2.00 [s, 3H, CH_3], 2.09 [m, 2H, CH_2], 2.32 [m, 2H, CH_2], 2.45 [s, 3H, N–CH_3], 3.03 [s, 1H, NH], 3.18 [m, 1H, Ar-H], 7.31 [m, 2H, Ar-H], 7.36 [t, 2H, Ar-H], 7.51 [s, 1H, NH] 9.04, ^{13}C-NMR (DMSO-d_6, ppm) [11.63, 29.28, 31.18, 31.94, 36.55, 41.55, 49.07, 50.99, 108.21, 123.83, 126.58, 129.53, 135.58, 152.95, 162.34, 171.94, 171.63], HRMS (Bruker Micro TOF) *m/z* [M + H, 437.25, M + Na, 459.24, M − H, 435.24].

*2.2.3.2. (**M2**).* *N*1-((*S*)-1-((3*S*,5*S*,7*S*)-Adamantan-1-yl)ethyl)-*N*4-(1,5-dimethyl-3-oxo-2-phenyl-2,3-dihydro-1*H*-pyrazol-4-yl)succinamide. Yield 97.5%, melting point 223–228 °C, solubility DMSO/DMF, IR cm^{-1}: [3302.06 N–H, 2896.68 N–H, 2847.62 C–H aromatic, 1655.69 C═O, 1639.20 C═O, 1541.09, 1308.83, 1221.42], ^{1}H-NMR Bruker 400 MHz (DMSO-d_6, ppm): [d, 3H, CH_3–CH], 0.93 [m, 6H, 3CH_2], 1.46 [m, 6H, 3CH_2], 1.64 [m, 3H, 3CH] 1.93 [s, 3H, CH_3], 2.09 [m, 2H, CH_2], 2.40 [m, 2H, CH_2], 2.50 [s, 3H, N–CH_3], 3.04 [m, 1H, CH], 3.54 [m, 3H, Ar-H], 7.36 [s, 1H, NH], 7.49 [m, 2H, Ar-H], 7.51 [s, 1H, NH] 9.05, ^{13}C-NMR (DMSO-d_6, ppm) [11.63, 14.69 28.27, 31.18, 31.37, 36.05, 36.56, 37.15, 38.41, 52.38, 108.24, 123.82, 126.57, 129.53, 135.58, 152.88, 162.32, 170.97, 171.64], HRMS (Bruker Micro TOF) *m/z* [M + H, 465.28, M + Na, 486.26, M − H, 463.27].

*2.2.3.3. (**M3**).* *N*1-(1,5-Dimethyl-3-oxo-2-phenyl-2,3-dihydro-1*H*-pyrazol-4-yl)-*N*4-((2*S*,4*R*)-1,7,7-trimethylbicyclo[2.2.1]heptan-2-yl)succinamide. Yield 95.8%, melting point 204–206 °C, solubility DMSO/DMF, IR cm^{-1}: [3356.88 N–H, 2951.58 C–H aromatic, 1674.05 C═O, 1630.65, 1580.77, 1529.52], ^{1}H-NMR Bruker 400 MHz (DMSO-d_6, ppm): [s, 3H, CH_3], 0.69 [s, 3H, CH_3], 0.83 [m, 2H, CH_2], 0.86 [m, 3H, CH_3] 0.89 [m, 2H, CH_2], 1.23 [m, 2H, CH_2], 2.40 [m, 1H, CH], 1.59 [m, 2H, CH_2], 1.70 [s, 3H, CH_3], 2.09 [m,2H, CH_2], 2.43 [m, 2H, CH_2], 2.49 [s, 3H, N–CH_3], 3.03 [m, 1H, CH] 4.10 [m, 3H, Ar-H], 7.34 [m, 2H, Ar-H], 7.50 [m, 1H, NH], 7.71 [s, 1H, NH] 9.04, ^{13}C-NMR (DMSO-d_6, ppm) [11.64, 14.33, 18.95, 20.24, 28.05, 28.23, 31.35, 36.10, 36.54, 44.86, 48.21, 49.78, 53.17, 108.20, 123.84, 126.59, 129.54, 135.57, 152.92, 162.33, 171.54, 171.70], HRMS (Bruker Micro TOF) *m/z* [M + H, 439.27, M + Na, 461.25, M − H, 437.25].

^{1}H-NMR, ^{13}C-NMR, COSY, HSQC, IR and HRMS spectra of all the synthesized compounds are available in SI (Fig. S1–S32).

2.3. Anticorrosion evaluation

2.3.1. Solution. The standard corrosion solution of 1.0 M HCl was made by diluting AR grade HCl (37%) with distilled water. This standard solution was used as a baseline for comparison. **M1–M3** were dissolved in 1.0 M HCl solutions to achieve the required concentrations (0.2, 0.4, 0.6, 0.8, and 1.0 mM).[37]

2.3.2. Weight loss analysis. An analytical balance with a precision of ±0.001 mg was used for the weight loss experiment. Prior to beginning each experiment, the mild steel coupon surface was cleaned using emery papers of various grades, such as 320, 660, and 1200. Acetone was used to degrease the coupons, and acetone and double-distilled water were used to rinse the coupons. Each coupon's weight was precisely determined after it had dried in warm air flow. The coupons were submerged in 30 mL of 1.0 M HCl solution in the absence and presence of various concentrations (0.2–1.0 mM) of the inhibitors (**M1–M3**) for varying time periods (1, 5, 12, 24, and 48 h) at controlled temperatures (30, 40, 50, and 60 °C) using an oven. After the experiment, the coupons were cleaned chemically to remove the corrosion products, involving immersion in 1.0 M HCl, rinsing with distilled water, propanone, and ethyl alcohol, drying with fast warm airflow, and precise re-weighing.[38,39] The chemical treatment referred to in the weight-loss section, involving a short immersion in 1.0 M HCl following ASTM/G1 practice, is only performed after gravimetric determinations for the removal of the bulk corrosion products and does not alter the surface-analysis data.[40,41]

2.3.3. Electrochemical analysis. All electrochemical measurements were performed on a Gamry electrochemical instrument using a three-electrode system. The Ag/AgCl electrode was used as the reference electrode, a graphite rod was used as the counter electrode while 4.0 cm^2 mild steel strips were used as the working electrode in all the electrochemical measurements. Before every experiment, the mild steel strips were pretreated similarly as in the weight loss experiment, including cleaning, degreasing, rinsing with water, and hot air drying. The working

electrode strips were immersed in 1.0 M HCl for 30 min to stabilize the open circuit potential (OCP) before each experiment.[39,42–45]

2.3.3.1. Potentiodynamic polarization (PDP). Potentiodynamic polarization (PDP) studies were conducted automatically across a potential range of −250 to +250 mV at open circuit potential (OCP) with a scan rate of 0.5 mV s^{-1}. All electrochemical analyses were performed at a constant temperature of 298 K. Tafel curves were obtained from the installed program of the gamry potentiostat.[43,46]

2.3.3.2. Electrochemical impedance spectroscopy (EIS). EIS experiments were recorded *via* excitation signals of 5 mV peak to peak amplitude at the corrosion potential by using the frequency range of 10^6 Hz to 0.1 Hz at the corresponding OCP in the Gamry Echem Analyst tool. Resistance parameters obtained from the Bode and Nyquist plots.[46,47]

2.3.4. Computational details

2.3.4.1. Structures preparation and optimization. Molecular geometries for the **M1**, **M2**, and **M3** inhibitors were generated in three dimensions using Avogadro software[48] and were subjected to initial geometric optimization using molecular mechanics to generate acceptable initial coordinates. Final electronic structure calculations were performed using density functional theory (DFT) with the ORCA (version 6.1) package.[49] To balance computational accuracy with efficiency for these large organic systems, the B3LYP/def2-SVP level of theory was selected.[50] Specifically, the def2-SVP basis set includes necessary polarization functions for heteroatoms, while the use of RIJCOSX approximations with the def2/J auxiliary basis allowed for rigorous geometry optimization in an aqueous medium (CPCM) without prohibitive computational costs.[51] The solvent effects of the acidic aqueous medium were incorporated to accurately represent the experimental conditions using the Conductor-Like Polarizable Continuum Model (CPCM) at 298.15 K (dielectric constant of water = 78.39).[52,53] After geometry optimization of all compounds, harmonic vibrational frequency analysis was performed at the same level of theory. The absence of any imaginary (negative) frequencies confirmed that the optimized structures represented the true energy minima on the potential energy surface. To ensure high-precision results for conceptual DFT reactivity descriptors, single-point energy calculations were performed at the more robust B3LYP/def2-TZVP level. This triple-zeta basis set was chosen to minimize basis set superposition error (BSSE) and provide a converged electronic density, which is critical for adsorption-related predictions. Grimme's D3BJ dispersion corrections were included to accurately account for the non-covalent interactions typical of inhibitor-metal interfaces. Following the vertical approximation, the energies (i) the neutral molecule [$E(N)$], (ii) the cation obtained by removing one electron [$E(N-1)$], and (iii) the anion obtained by adding one electron [$E(N+1)$]. The cation and anion calculations were performed as single-point calculations at the optimized geometry of the neutral molecule. Atomic partial charges were further evaluated using Mulliken population analysis to identify potential nucleophilic and electrophilic adsorption sites.[54,55]

2.3.4.2. Quantum chemical descriptors calculations. The quantum chemical descriptor in terms of the vertical ionization potential (I_v) and 0 vertical electron affinity (A_v) was determined according to the following equations.[56]

$$I_v \approx E(N-1) - E(N) \quad (1)$$

$$A_v \approx E(N) + E(N+1) \quad (2)$$

Here, $E(N)$ is the total energy of the optimized structures, and $E(N-1)$ and $E(N+1)$ stand for the cation and anion energies in the optimized neutral geometries, respectively. Using the I_v and A_v values, the energy gas ($\Delta E_g = I_v - A_v$) value was calculated.[57] The HOMO and LUMO energies were computed and used to measure the energy gap (ΔE_{gap}) of the compounds as follows:

$$\Delta E_{gap} = E_{LUMO}E_{HOMO} \quad (3)$$

The electronegativity (χ), hardness (η), softness (S), chemical potential (Π) and nucleophilicity (ω) were evaluated using the following expressions, eqn (4)–(9):[58,59]

$$\chi = (I + A)/2 \quad (4)$$

$$\eta = (I - A)/2 \quad (5)$$

$$S = \eta - 1 \quad (6)$$

$$\Pi = -1/2(I_v + A_v) \quad (7)$$

$$\omega = \chi^2/2\eta \quad (8)$$

$$\varepsilon = 1/\omega \quad (9)$$

To determine the fractional number of electrons transferred (ΔN), we utilized the following eqn (10) from the ref. 60.

$$\Delta N = (\chi_{Fe} - \chi_{inh})/(2(\chi_{Fe} + \chi_{inh})) \quad (10)$$

eqn (11)[61,62] was developed based on the findings obtained from the determination of iron's electronegativity (7 eV) and hardness (0 eV).

$$\Delta N = (7 - \chi_{inh})/(2(\chi_{inh})) \quad (11)$$

Additionally, Gomez *et al.*[63] defined the electronic back-donation energy as eqn (12):

$$\Delta E_{b-d} = -\eta_{inh}/4 \quad (12)$$

In eqn (12), if $\Delta E_{b-d} \leq 0$, then the process is energetically favored.

2.3.4.3. Fukui indices and dual Fukui descriptors calculations. The local sites' reactivity responsible for interactions with the Fe-surface were investigated using the local Fukui indices condensed local softness (σ_k^a), and local electrophilicity (ω_k^a), according eqn (13):

$$\begin{aligned} (f_k^+) &= q_k^{(N+1)} - q_k^{(N)} \quad \text{(for nucleophilic attacks)} \\ (f_k^-) &= q_k^{(N)} - q_k^{(N-1)} \quad \text{(for electrophilic attacks)} \\ (\sigma_k^a) &= S(f_k^a) \quad \text{and } (\omega_k^a) = \omega(f_k^a) \end{aligned} \quad (13)$$

where $q_k^{(N)}$, $q_k^{(N+1)}$, and $q_k^{(N-1)}$ are the charges values of atom k for neutral, cation and anion, respectively. The α = + and − denotes

local softness quantities for nucleophilic, electrophilic, and radical attacks, respectively. More specifically, the dual Fukui descriptor or second order Fukui functions (f_k^2), their associated dual local softness ($\Delta\sigma_k$) and dual local philicity ($\Delta\omega_k$) was used to provide a simplistic and instinctive method to local chemical reactivity. The definitions of these dual descriptors are followed as seen below in eqn (14)–(16)

$$f_k^2 = f_k^+ - f_k^- \quad (14)$$

$$\Delta\sigma_k = \sigma_k^+ - \sigma_k^- \quad (15)$$

$$\Delta\omega_k = \omega_k^+ - (\omega_k^-) \quad (16)$$

2.3.5. Surface analysis. To perform SEM, EDX, FESEM, and XPS analyses, mild-steel coupons were dipped into 1.0 M HCl with or without a 1.0 mM inhibitor for 5.0 hours.[53,64–66] The coupons were then gently rinsed with distilled water and absolute ethanol to remove loose corrosion products or excess electrolyte, thereby keeping the adsorbed inhibitor film intact. The coupons were immediately dried under a hot-air stream. In the methodology, the 1.0 M HCl cleaning step was used only for the gravimetric/weight-loss coupons, where removal of corrosion products before final weighing is required.[67] In contrast, the coupons used for surface characterization (SEM/FESEM/XPS) were handled separately: after immersion, they were washed with distilled water and ethanol and then dried before analysis, rather than being acid-cleaned.[68]

3. Results and discussion

3.1. Spectroscopic characterization of synthesized compounds

The 4-aminoantipyrine (**2**) was synthesized with efficient yield (98%) from (**1**) through the acid hydrolysis. The ^{1}H-NMR spectrum (Fig. S1) of as-synthesized (**2**) shows the 1H multiplet and 4H multiplets in the aromatic region (7.23 ppm and 7.44 ppm respectively) which confirm the five aromatic protons. The two 3H singlets of methyl groups at 2.09 ppm (C–CH_3) and 2.73 ppm (N–CH_3) confirm the pyrazolone ring in the structure. The 2H singlet at 3.84 ppm indicate the NH_2 group on the pyrazolone ring of 4-aminoantipyrine (**2**). The ^{13}C-NMR spectrum (Fig. S2) shows the nine non-equivalent carbons peaks at 10.38, 38.79, 120.58, 122.31, 125.58, 129.39, 135.95, 136.09, 161.89 ppm. Here the peaks at 10.38 and 38.79 ppm indicate the two methyl groups C–**C**H_3 and N–**C**H_3 respectively on the pyrazolone ring. The peaks at 161.89 ppm indicate the C═O group, 135.95 ppm CH_3–C═C and 120.58 H_2N–C═C of pyrazolone ring. The remaining peaks at 122.58, 125.58, 129.39 and 136.09 indicate the four non-equivalent aromatic carbons in the structure of **2**. The COSY experiment (Fig. S3) shows H–H couplings and HSQC experiment (Fig. S4) C–H correlation in the structure. Through COSY and HSQC experiments the proton–proton and proton–carbon connectivities were confirmed. Furthermore, the high-resolution mass spectrometry (HRMS) spectrum (Fig. S5) shows M + H and M + Na peaks at *m/z* 204.11 and 226.09, respectively also proving the synthesis of 4-aminoantipyrine (**2**).

The compound **4** was synthesized from **2** and **3** as shown in Scheme 1. The FT-IR spectrum of **4** (Fig. S6) shows bands (cm^{-1}) at 3283 (NH amide), 2929 (OH of carboxylic acid broad), 1741 (C═O), 1666 (C═O), 1615 (C═C) and 1600 (C═O) which indicate the presence of carboxylic acid, amide, alkene and ketonic linkages in the structure. The ^{1}H-NMR spectrum of **4** (Fig. S7) shows the elimination of the NH_2 peak of 2H singlet at 3.84 ppm of compound **2**, with an additional NH (amide) peak of 1H singlet at 9.11 ppm, indicating the formation of an amide linkage. Furthermore, this spectrum also shows 4H multiplets of C**H**$_2$–C**H**$_2$ at 2.51 ppm and a 1H broad singlet of COO**H** at 12.10 ppm, indicating the synthesis of the acid derivative of 4-aminoantipyrine (**4**). The ^{13}C-NMR spectrum (Fig. S8) also shows thirteen non-equivalent carbons at 11.65, 29.54, 30.34, 36.54, 108.16, 123.86, 126.61, 129.54, 135.56, 152.89, 162.31,

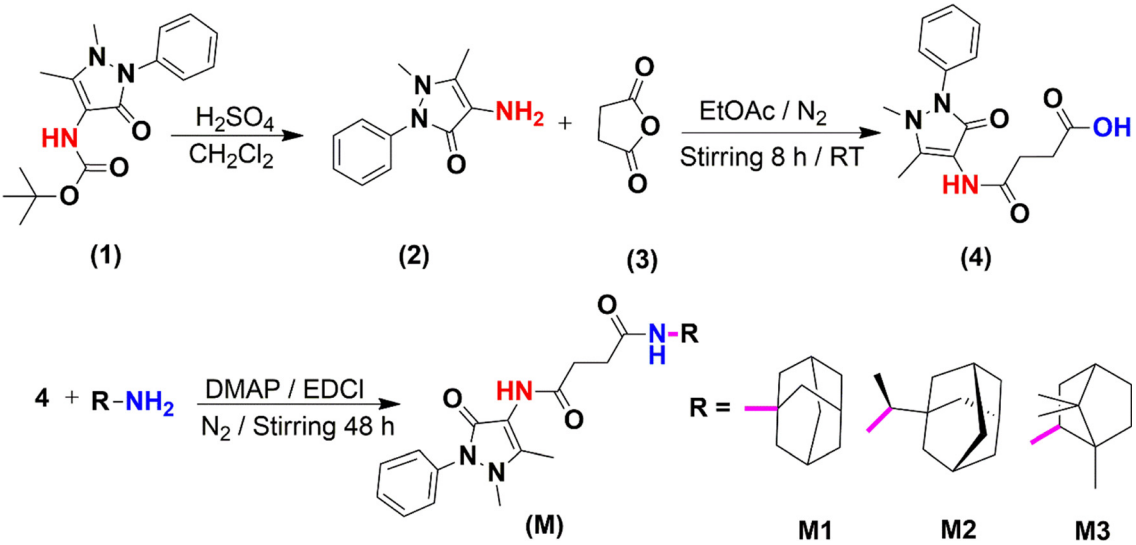

Scheme 1 Schematic representation of the synthetic pathway for corrosion inhibitor molecules of 4-aminoantipyrine derivatives **M1**, **M2** and **M3**.

171.09, 174.26 ppm. This spectrum shows two additional aliphatic carbons (**C**H_2–**C**H_2) at 29.54, 30.34 ppm, NH–**C**=O at 171.09 ppm, and **C**OOH at 174.26 ppm peaks to compound **2**. The H–H and H–C correlations are also confirmed by COSY (Fig. S9) and HSQC (Fig. S10) spectra respectively. The HRMS spectrum (Fig. S11 and S12) shows M + Na and M − H peaks at *m/z* 326.11 and 302.11, respectively, also justify the synthesis of the acid derivative of 4-aminoantipyrine (**4**).

The new amide derivatives **M1–M3** were synthesized from **4**. FT-IR was performed to analyze the formation of **M1** as shown in Fig. S13. Formation of the amide function group in **M1** appears at 2904 cm^{-1} (NH amidic sharp) while the broad band of acid at 2929 cm^{-1} in **4** was eliminated. Similarly, **M2** and **M3** (Fig. S14 and S15) shows new vibration bands (NH amidic sharp) at 2896 cm^{-1} and 2851 cm^{-1}, respectively. The appearance of the NH band indicates the successful formation of amide linkage in **M1**, **M2**, and **M3**. The stronger band Likewise, in **M1**, **M2**, and **M3**, sharp vibration bands (C=O amidic) at 1643 cm^{-1}, 1639 cm^{-1}, and 1630 cm^{-1}, respectively, indicate the formation of amide linkages. As the presence of electron-donating groups and greater steric hindrance increases the electron density around the bond, it results in weaken bonds and decrease in the vibrational frequency, therefore, the amidic vibration bands (NH and C=O) of **M2** and **M3** appear at lower wavenumbers with high intensity compared to **M1**. As expected for amide formation, the N–H stretching band appears at 3358 cm^{-1} (**M1**), 3302 cm^{-1} (**M2**), and 3357 cm^{-1} (**M3**). The red shift of 56 cm^{-1} is observed for **M2** can be explained by higher electron density at the amide nitrogen as a result of the α-methyl substitution on the adamantyl cage, weakening the N–H bond through steric crowding and hyperconjugation (the typical $\Delta\nu$ NH range for these effects: 30–60 cm^{-1}) combination.[69] The C=O stretching frequencies are 1643 cm^{-1} (**M1**), 1656/1639 cm^{-1} (**M2**), and 1674/1631 cm^{-1} (**M3**) correspondingly. The components at lower frequency in **M2** and **M3** ($\Delta\nu$ C=O ≈ −4 to −12 cm^{-1} relative to **M1**) are the result of a slight decrease in carbonyl bond order as the alkyl substituents on the adamantyl moiety acting as electron donor increase the resonance between the nitrogen lone pair. These little, yet consistent with the literature shifts indicate that large conformational changes are not revealed by the sterically modulated amides.[70,71]

To further confirm the formation of as-synthesized **M1**, **M2** and **M3**, the ^{1}H-NMR spectra for **M1**, **M2** and **M3** (Fig. S16–S18) were recorded. The elimination of the COO**H** broad peak of 1H singlet at 12.10 ppm of compound **4** with additional N**H** (amide) peaks of 1H singlet at 3.03 ppm, 7.49 ppm, and 7.71 ppm, respectively, indicates the formation of new amide linkages. The steric factor in the **M2** and **M3** explains the different peak positions in the spectrum. The aliphatic region of the ^{1}H-NMR spectrum of **M1** contains additional 6H multiplets of 3CH_2 at 1.60 ppm, 6H multiplets of 3CH_2 at 1.92 ppm, and 3H multiplets of 3CH at 2.00 ppm indicate the adamantyl group in the structure. The aliphatic region of ^{1}H-NMR spectrum of **M2** shows 3H doublet of C**H**$_3$–CH at 0.93 ppm, 6H muliplets of 3C**H**$_2$ at 1.46 ppm, 6H multiplets of 3C**H**$_2$ at 1.64 ppm, 3H mutiplets of 3C**H** at 1.93 ppm and 1H multiplet of CH_3–C**H** at 3.54 ppm which indicate adamantyl derivative group in the structure. The spectrum of **M2** shows the additional two peaks of 3H doublet of C**H**$_3$–CH at 0.93 ppm and 1H multiplet of CH_3–C**H** at 3.54 ppm compared to **M1** molecule which justify the structure of **M2**. The aliphatic region of ^{1}H-NMR spectrum of **M3** also shows 3H singlet of C**H**$_3$–C at 0.69 ppm, 3H singlet of C**H**$_3$–C at 0.83 ppm, 2H muliplet of C**H**$_2$ at 0.86 ppm, 3H multiplet of C**H**$_3$ at 0.89 ppm, 2H mutiplets of C**H**$_2$ at 1.23 ppm, 2H mutiplets of C**H**$_2$ at 1.40 ppm, 1H mutiplets of C**H** at 1.59 ppm and 1H multiplet of C**H** at 1.70 ppm which indicate alkylated adamantyl group in the structure. The structure of **M3** contains more three methyl groups on the adamantyl as compared to **M1**. The spectrum of **M3** shows 3H singlet of C**H**$_3$–C at 0.69, 3H singlet of C**H**$_3$–C at 0.83 and 3H multiplet of C**H**$_3$ at 0.89 pm of these three methyl groups on the adamantly, justifying the structure of **M3**.

The ^{13}C-NMR spectrum of **M1** (Fig. S19) shows thirteen non-equivalent carbons at 11.63, 29.28, 31.18, 31.94, 36.55, 41.55, 49.07, 50.99, 108.21, 123.83, 126.58, 129.53, 135.58, 152.95, 162.34, 171.94 and 171.63 ppm. This spectrum bears four aliphatic additional carbons at 31.94, 41.55, 49.07 and 50.99 ppm confirming the adamentyl group in the structure. The ^{13}C-NMR spectrum of **M2** (Fig. S20) also shows thirteen non-equivalent carbons at 11.63, 14.69 28.27, 31.18, 31.37, 36.05, 36.56, 37.15, 38.41, 52.38, 108.24, 123.82, 126.57, 129.53, 135.58, 152.88, 162.32, 170.97 and 171.64 ppm. This spectrum has six aliphatic additional carbons at 14.69, 31.37, 36.05, 37.15, 38.41 and 52.38 ppm confirming the adamantly group in the structure. The ^{13}C-NMR spectrum (Fig. S21) of **M3** also shows twenty-two non-equivalent carbons at 11.64, 14.33, 18.95, 20.24, 28.05, 28.23, 31.35, 36.10, 36.54, 44.86, 48.21, 49.78, 53.17, 108.20, 123.84, 126.59, 129.54, 135.57, 152.92, 162.33, 171.54 and 171.70 ppm. This spectrum bears nine aliphatic additional carbons at 14.33, 18.95, 20.24, 28.05, 36.10, 44.86, 48.21, 49.78 and 53.17 ppm confirming the alkylated adamantly in the structure. The aliphatic signals of **M1**, **M2** and **M3** spectrums create main difference and confirm their structures. The ^{13}C spectra of **M1**, **M2** and **M3** having 4, 6 and 9 non-equivalent carbons indicate the structural differences and confirm the structure of the synthesized compounds.

The H–H and H–C correlations of **M1–M3** are also confirmed by COSY (Fig. S22 and S23) and HSQC (Fig. S24–S26) spectrums. Furthermore, The HRMS spectrum of **M1**, **M2** and **M3** (Fig. S27–S32) shows M + H, M + Na and M − H peaks at *m/z* 437.25, 459.24 and 435.24 respectively **M1**, 465.28, 486.26 and 463.27 respectively **M2**, and 439.27, 461.25 and 437.25 respectively **M3** also proving the formation of **M1**, **M2** and **M3**.

3.2. Anticorrosion measurements

The as-synthesized inhibitors were undergoes the anticorrosion analysis by weight loss and electrochemical measurements. The weight loss method was used to determine the effect of time, concentration and temperature on the corrosion inhibition properties of inhibitors. In the electrochemical method, the potentiodynamic polarization (PDP) curves *via* tafel plots and electrochemical impendence spectroscopy (EIS) *via* nyquist, bode and phase angle plots were used for anticorrosion evaluations.

For these analyses, the required concentration inhibitors weight was dissolved in the 1.0 M HCl solution. All the inhibitors dissolved partially in pure water while clearly dissolved in acidic medium at room temperature due to protonation of nitrogen in the structure of inhibitors. Solubility tests showed that all three compounds were fully dissolving (>1.0 mM) when stirring at 298 K, so heating or sonication are not required at these low concentrations. Subsequent filtration revealed no evidence of precipitation, confirming the stability of the prepared solutions.[24,72]

3.2.1. Weight loss evaluation

3.2.1.1. Effect of concentration. These experiments were conducted to analyze the potential of the as-synthesized compounds in preventing the corrosion. The rate of corrosion (C_R), loss of weight with time, coverage of surface with inhibitors (θ) and efficiency of corrosion inhibition (IE%) for **M1**, **M2** and **M3** are tabulated in Table S1. Findings from these experiments facilitate the identification of the optimal inhibitor concentration for corrosion prevention and enable a comparative analysis of the synthesized inhibitors (**M1–M3**) with respect to their corrosion parameters.

The as-synthesized compounds were adsorbed on the exposed surface of MS coupons and block the reactive sites of the metal from corrosion that leads to a slow in the C_R. The unoccupied sites on the surface of iron coupons are susceptible to corrosion, and the sites blocked by inhibitors will not undergo corrosion.[73,74] The C_R of MS coupons were calculated through these analyses after 5.0 h at 303 K by using eqn (17).

$$C_R = \frac{W}{\rho \alpha t} \tag{17}$$

C_R is the rate of corrosion of the MS strips, W is the decrease of weight of MS strips (g), ρ is the density (g cm^{-3}), α is the exposed surface area (cm^2) and t is the submerged time (h).

The corrosion rate $C_{R(o)}$ of the iron coupons in the absence of inhibitors is 2.94×10^{-3} cm h^{-1} shown indicating that unblocked iron sites are susceptible to corrosion under 1.0 M HCl environment. However, the addition of 0.2 mM of **M1** as an inhibitor decreases the corrosion rate to $5.02 \times 10^{-4} \pm 1.0 \times 10^{-05}$ cm h^{-1}, as shown in Fig. 1a. It was observed that by increasing concentration to 1.0 mM, the C_R decrease to $6.02 \times 10^{-5} \pm 1.2 \times 10^{-06}$ cm h^{-1}. The C_R slows down with rise of concentration reveals the **M1** molecule interacts with the iron sites to block them from corrosion. It can be assumed that by the rise in concentration of **M1–M3** will enhances the adsorption of organic compounds on the surface of MS coupons.

The C_R of **M2** and **M3** was determined under the same conditions. The C_R of iron coupons in 0.2 mM solutions of **M2** (Fig. 1b) and **M3** (Fig. 1c) were $1.03 \times 10^{-3} \pm 2.1 \times 10^{-05}$ cm h^{-1} and $7.31 \times 10^{-4} \pm 1.5 \times 10^{-05}$ cm h^{-1}, respectively. The C_R of **M2** and **M3** were further decreased by increasing their concentrations. The C_R of iron coupons in 1.0 mM solutions of **M2** and **M3** were $4.44 \times 10^{-4} \pm 8.9 \times 10^{-06}$ cm h^{-1} and $1.47 \times 10^{-4} \pm 2.9 \times 10^{-06}$ cm h^{-1} respectively. It was showed by the experimental data that C_R decreases by raising the concentration of inhibitors (**M1–M3**). Among **M1–M3**, **M1** exhibits the lowest C_R owing to its molecular structure, which presents minimal steric hindrance to the adamantly group. This suggests that **M1** covers the surface of the iron coupon more effectively. The presence of alkyl groups on the adamantly moiety in **M2** and **M3** induces steric hindrance, thereby limiting the electron-donating capacity of the heteroatoms (N and O) within their structures. To further evaluate the performances of **M1**, **M2**, and **M3**, the θ of the inhibitors was measured using eqn (18).[37]

$$\theta = 1 - \frac{C_{R(i)}}{C_{R(o)}} \tag{18}$$

Here, $C_{R(i)}$ shows the corrosion rate with inhibitors, and $C_{R(o)}$ shows the corrosion rate without inhibitor. The θ of inhibitors can also be correlated with their inhibition efficiency (IE%) in eqn (19).

$$\text{IE\%} = \theta \times 100 \tag{19}$$

Fig. 1a–c presents the IE% and Table S1 summarize the results of θ and IE% of inhibitors (**M1–M3**) related to their concentrations (C_{inh}). At lower concentrations, the C_R decreases rapidly and stabilizes after some time, whereas the IE% enhances before the formation of smooth layer of the inhibitors on the metallic surface. These trends are attributed to the adsorption of **M1–M3**, which forms a protective film that mitigates corrosion. Notably, all three compounds exhibit good inhibitive performance, even at low concentrations (0.2 mM), and maintain their performance across the entire concentration range. They owe their effectiveness to the presence of extensive amide linkages in the structure, which facilitate strong interactions between the as-synthesized compounds and the surface of MS strips, as further evidenced by surface analysis (SEM, FESEM,

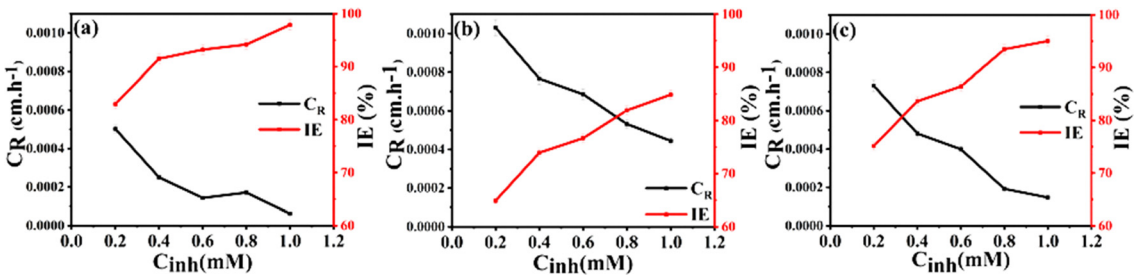

Fig. 1 Effect of concentration (mM) on IE% and C_R of MS coupons immersed in (a) **M1**, (b) **M2** and (c) **M3** for 5.0 hours.

EDX, and XPS). The **M1** (0.2 mM) shows θ and IE% of 0.830 ± 0.02 and 82.93 ± 1.6, respectively. Further increase in **M1** concentration increases surface coverage (θ) and IE%. At 1.0 mM concentration of **M1**, the θ value increases to 0.980 ± 0.02, and IE% increases to 97.89 ± 1.9. Likewise, the θ and IE% of **M2** at 0.2 mM are 0.650 ± 0.01 and 64.85 ± 1.3 respectively, whereas, at 1.0 mM concentration, θ and IE% further increase up to 0.850 ± 0.02 and 84.88 ± 1.7 respectively at a concentration of 1.0 mM. The θ and IE% of **M3** at 0.2 mM are 0.750 ± 0.01 and 75.13 ± 1.5, while at 1.0 mM they are 0.950 ± 0.02 and 95.02 ± 1.9. Among these synthesized inhibitors, **M1** shows the highest θ and IE compared to **M2** and **M3**. The **M3** has a higher θ and IE% than **M2** but lower than **M3**. The lower values of C_R, higher values of θ and IE% of **M1** is due to the lower steric hindrance of adamantly group for heteroatoms (O and N) than in case of **M2** and **M3**. The non-substituted adamantly group of **M1** enables the lone pairs of the heteroatoms (O and N) to be more donate able for adsorption on mild steel than to the steric hindered heteroatoms (O and N) of **M2** and **M3**.

3.2.1.2. Effect of immersion time. The C_R, θ and IE% of MS strips adsorbed by organic inhibitors **M1–M3** in the acidic medium were also affected by immersion time. The experiments were performed for 48.0 h immersion time at constant temperature of 303 K with **M1–M3** concentrations ranges from 0.2 to 1.0 mM.

Results are shown in Fig. 2a–f and Table S2, revealing the C_R of **M1–M3** significantly reduced by increasing their concentrations 0.2 to 1.0 mM. Higher concentrations of **M1–M3** prove more effective in mitigating corrosion. The θ and IE% increases as the immersion time increases at constant inhibitor concentration (**M1–M3**). C_R of MS coupons in blank 1.0 M HCl is 4.62×10^{-4} cm h^{-1} after 1.0 h immersion time. C_R of steel coupons in 0.2 mM **M1** solution after 1.0 h immersion time is $1.71 \times 10^{-4} \pm 3.4 \times 10^{-06}$ cm h^{-1} as shown in Fig. 2a, b and Table S2. The corrosion rates further decreases to $9.23 \times 10^{-5} \pm 1.8 \times 10^{-06}$ cm h^{-1} in the same immersion time as the concentration of **M1** inhibitor enhanced up to 1.0 mM. Likewise, IE% of **M1** increases from 59.80 ± 1.2 to 78.35 ± 1.6 by increasing its concentration from 0.2 mM to 1.0 mM respectively, after 1.0 h exposure time. The other two inhibitors (**M2** and **M3**) show the same trends of C_R and IE% upon increasing the concentration up to 1.0 mM, as summarized in Fig. 2c–f and Table S2. For **M2**, C_R decreases $2.92 \times 10^{-4} \pm 5.8 \times 10^{-06}$ cm h^{-1} to $1.24 \times 10^{-4} \pm 2.5 \times 10^{-06}$ cm h^{-1} and IE% increases 31.60 ± 0.6 to 70.91 ± 1.4 as the concentration rose 0.2 to 1.0 mM after 1.0 h exposure time. Similarly, C_R and IE% of **M3** were $2.37 \times 10^{-4} \pm 4.7 \times 10^{-06}$ cm h^{-1} and 44.53 ± 0.9 at 0.2 mM while $1.14 \times 10^{-4} \pm 2.3 \times 10^{-06}$ cm h^{-1} and 73.18 ± 1.5 respectively at 1.0 mM concentration for 1.0 h immersion time. Notably, the IE% of **M1–M3** also exhibits a time-dependent pattern. Increasing the immersion time, results in the decrease in C_R and increase in IE%. The present analysis evaluates C_R, θ and IE% of the mild steel up to 48 h. C_R in **M1** decreases from $1.71 \times 10^{-4} \pm 3.3 \times 10^{-06}$ cm h^{-1} to $1.83 \times 10^{-6} \pm 3.7 \times 10^{-08}$ cm h^{-1} and IE% raises from 59.80 ± 1.2 to 96.43 ± 1.9 during 1.0 to 48 h immersion time, respectively, in 0.2 mM solution. Similarly, C_R of steel coupons in similar concentration of **M2** decreases from $2.92 \times 10^{-4} \pm 5.8 \times 10^{-06}$ cm h^{-1} to $1.07 \times 10^{-5} \pm 2.1 \times 10^{-07}$ and IE% increases 31.60 ± 0.6 to 79.20 ± 1.6 in 1.0 to 48 h, respectively. The third inhibitor **M3** also follows the same trend of C_R ($2.37 \times 10^{-4} \pm 4.7 \times 10^{-06}$ cm h^{-1} to $5.07 \times 10^{-6} \pm 1.0 \times 10^{-07}$ cm h^{-1}), θ (0.450 ± 0.01 to 0.900 ± 0.02) and IE% (44.53 ± 0.9 to 90.11 ± 1.8) during 1.0 to 48.0 h in 0.2 mM solution. As the immersion time increases from 1.0 to 48 h, the corrosion rate consistently decreases, suggesting that extended exposure to **M1–M3** enhances their inhibition effect.

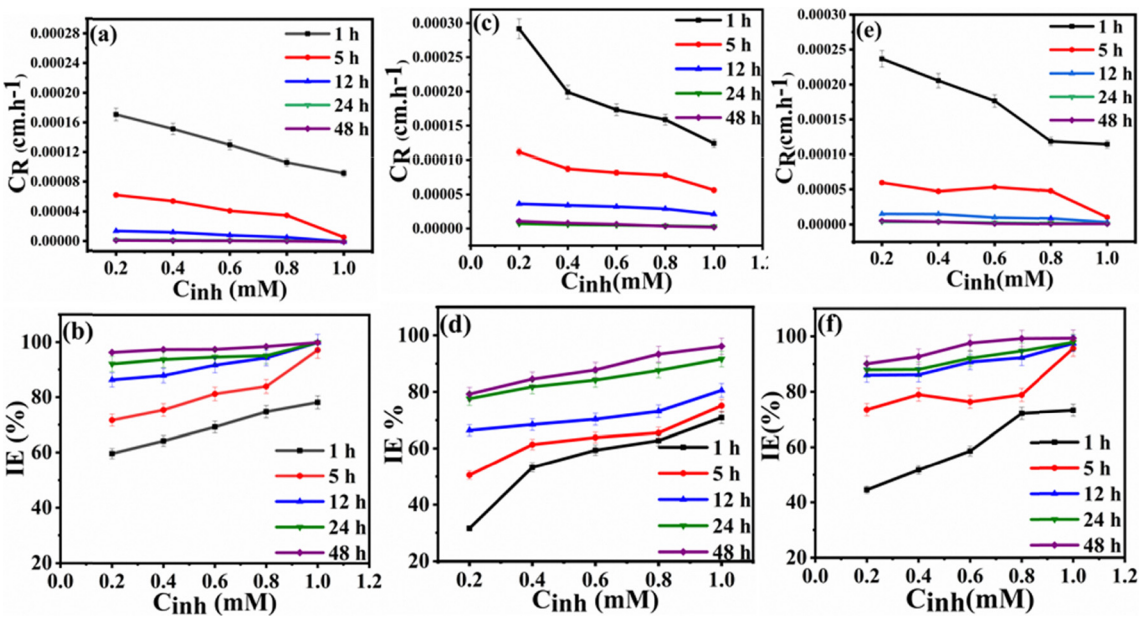

Fig. 2 Effect of time on C_R and IE% of MS coupons adsorbed by inhibitors (a) and (b) **M1**, (c) and (d) **M2** and (e) and (f) **M3**.

For example, at concentration of 1.0 mM of **M1–M3**, **M1** exhibits 100 ± 2.0 IE% after 12 h of immersion, whereas **M2** and **M3** achieve 80.54 ± 1.6 and 97.48 ± 1.9 IE% after 12 h. The most significant effect is observed at the highest concentration (1.0 mM), resulting in IE% of 100 ± 2.0 for **M1**, 96.12 ± 1.9 for **M2**, and 99.33 ± 1.9 for **M3** after 48 h. In contrast, at a concentration of 0.2 mM, the IE% are 96.43 ± 1.9 for **M1**, 79.20 ± 1.6 for **M2**, and 90.11 ± 1.8 for **M3** after 48 h. A significant observation is made after 24 hours of immersion, when the IE% of **M1–M3** begins to decline gradually due greater surface coverage with inhibitors. The IE% of **M1–M3** also depends on the pH of medium, concentration of solution and temperature.[75]

3.2.1.3. Effect of immersion temperature. These experiments were designed to assess the thermal stability and IE% at elevated temperatures of the synthesized inhibitors. The corrosion rates and inhibition efficiencies of **M1–M3** were evaluated using the mass reduction technique after a 5.0 h exposure time and temperatures changes 30 °C to 60 °C.

Increasing temperature results in an elevated corrosion rate and a reduced efficiency of **M1–M3** inhibitors. At all concentrations, the IE% of **M1–M3** reduced by raising the temperature, indicative of a physisorption process.[76,77] Fig. 3a–f and Table S3 illustrates the change of temperature effects on the C_R and IE% of MS coupons in acidic medium. At a temperature of 303 K, the bare MS coupon shows the C_R value of 1.36×10^{-3} cm h^{-1}. However, 0.2 mM of **M1** addition decreases C_R to $4.96 \times 10^{-4} \pm 9.9 \times 10^{-06}$ cm h^{-1} and IE% 63.65 ± 1.3. On the other hand, the C_R of **M1** further increase by raising the temperature increases the C_R at the same concentration of 0.2 mM. Likewise, the same trend is observed for all the concentrations of **M1**. At 1.0 mM concentration of **M1**, the corrosion rate decreases to $1.59 \times 10^{-4} \pm 3.2 \times 10^{-06}$ cm h^{-1}, and IE% increases to 88.4 ± 1.8 at 303 K, as shown in Fig. 3a and b. However, upon further increase in temperature to 333 K, C_R of 1.0 mM solution of **M1** increases to $1.14 \times 10^{-3} \pm 2.3 \times 10^{-05}$ cm h^{-1}, while the IE% decreases to 76 ± 1.5. The same trend appears with **M1** and **M2** as shown in Fig. 3c–f. The 1.0 mM solution of **M2** demonstrates an IE% of 73.1 ± 1.5 at 303 K, decreasing to 57.4 ± 1.1 at 333 K, as shown in Table S3, Fig. 3c and d. **M3** shows an IE% of 79.5 ± 1.6 at 303 K, which declines to 65.6 ± 1.3 at 333 K when the inhibitor concentration is 1.0 mM, as shown in Table S3, Fig. 3e and f.

To understand the adsorption of inhibitors (**M1–M3**) on MS strips surface in the acidic medium at different temperature (303 K to 333 K), the other thermodynamic parameters like activation energy (E_a), enthalpy change (ΔH), entropy change (ΔS) and Gibb's free change (ΔG) were determined by using eqn (20)–(23). Arrhenius equation (eqn (20)) used to calculate the activation energy (E_a) of the inhibitors. Where T = temperature (K), R = gas constant (8.314 J K^{-1} mol^{-1}), and A is the Arrhenius constant. By plotting the graph between $\ln C_R$ *vs.* $1/T$, the slope = $-E_a/R$ and the intercept = $\ln A$. The E_a can easily calculate from the slope.[37]

$$\ln C_R = \ln A - \left(\frac{E_a}{RT}\right) \quad (20)$$

By using the above eqn (20), the E_a of inhibitors (**M1–M3**) calculated were summarized in Table 1, Table S4 and Fig. 4a, c, e. All the Arrhenius curves gives the R^2 values near to unity justify the good fittings.

The **M1**, **M2** and **M3** give the E_a values of 52.36 kJ mol^{-1}, 54.83 kJ mol^{-1} and 51.29 kJ mol^{-1} respectively at their 0.2 mM solutions. The E_a values of all the inhibitors decreases by raising the concentration of as-synthesized inhibitors show

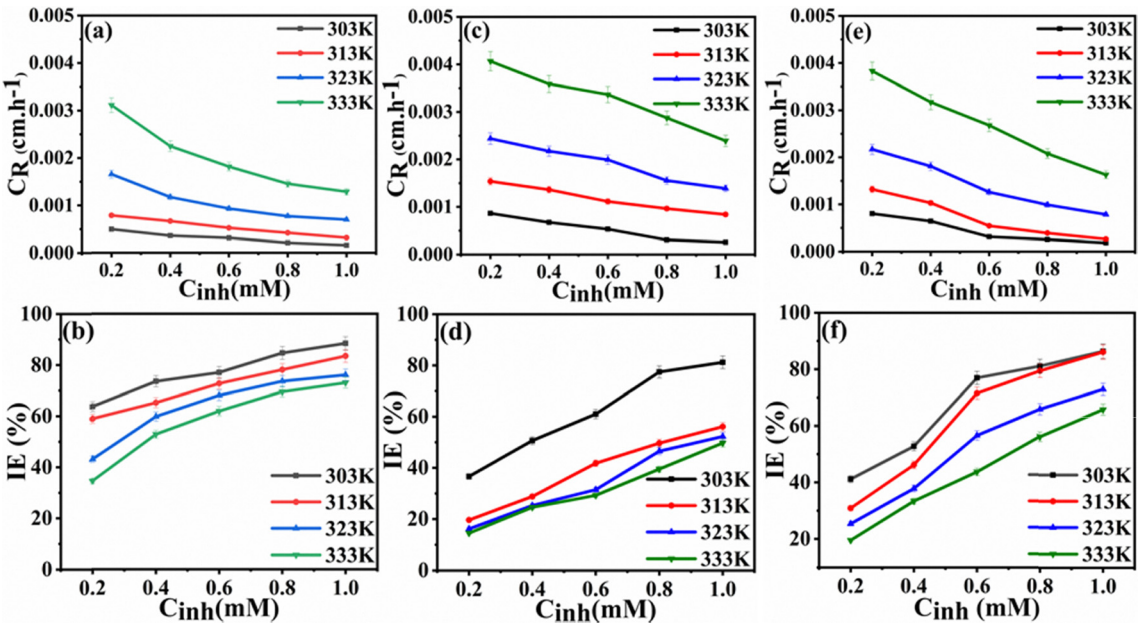

Fig. 3 Effect of temperature on C_R and IE% of MS coupons adsorbed by inhibitors in acidic medium for 5.0 h exposure time (a) and (b) **M1**, (c) and (d) **M2** and (e) and (f) **M3**.

Table 1 Activation energy (E_a) values at various concentration of inhibitors (**M1–M3**) along with fitting parameters

Concentration (mM)	Slope	Intercept	R^2	E_a (kJ mol^{-1})
M1				
0.2	−6297.45	13.09 ± 1.5	0.99	52.36
0.4	−6095.47	12.17 ± 0.6	0.99	50.68
0.6	−5881.72	11.29 ± 1.2	0.99	48.90
0.8	−5442.33	9.71 ± 1.3	0.98	45.25
1.0	−5316.29	9.13 ± 1.3	0.98	44.20
M2				
0.2	−6594.57	14.44 ± 1.0	0.99	54.83
0.4	−6506.76	13.96 ± 0.1	0.99	54.10
0.6	−6332.27	13.21 ± 0.8	0.99	52.65
0.8	−6266.21	12.88 ± 1.0	0.99	52.10
1.0	−6002.64	11.88 ± 1.7	0.98	49.91
M3				
0.2	−6169.48	12.82 ± 0.9	0.99	51.29
0.4	−5945.32	11.79 ± 0.6	0.99	49.43
0.6	−5836.7	11.21 ± 1.4	0.98	48.53
0.8	−5777.46	10.90 ± 1.9	0.97	48.03
1.0	−5637.06	10.33 ± 2.2	0.97	46.87

the ease of adsorption of inhibitors on the surface MS strips at elevated concentration. The E_a of **M1**, **M2** and **M3** decreases to 44.20 kJ mol^{-1}, 49.91 kJ mol^{-1} and 46.87 kJ mol^{-1} respectively at 1.0 mM solutions. Our inhibitors represent the E_a values less than 80 kJ mol^{-1} threshold, support the physisorption adsorption mechanism.[78] The high efficiency of **M1** can be explained by the fact that it adsorbs strongly on the metal surface, and this may be attributed to less steric hindrances on the electron rich sites such as heteroatoms like nitrogen and oxygen. The presence of such sites enables the donation of an electron to the metal surface, thus forming a stable and compact film that prevents the corrosive substances from reaching the metal surface. The moderate inhibition efficiency of **M3** indicates that the compound adsorbs on the metal surface but with low adsorption strength compared to that of compound **M1**. This may be attributed to the fact that the compound has fewer adsorption sites due to presence of alkyl substitution on the adamantyl group causes steric hindrance and an unfavorable orientation for adsorption, thus forming a less compact film that allows the corrosive substances to reach the metal surface. On the contrary, the least inhibition efficiency of **M2** may be attributed to the fact that the compound adsorbs weakly on the metal surface. This may be attributed to the fact that the compound has structural limitations such as fewer electron-donating sites due to more steric hinderance, thus forming a less stable film that allows the corrosive substances to reach the metal surface and react with it.

The ΔH and ΔS were calculated by using eqn (21) shown in Table 2 along with fitting parameters.[79–81] In this context, ΔS and ΔH denote the changes in entropy and enthalpy of activation respectively, where h is Planck's constant and N is the Avogadro's constant.[37]

$$C_R = \left(\frac{RT}{Nh}\right) \exp\left(\frac{\Delta S}{R}\right) \exp\left(\frac{\Delta H}{RT}\right) \quad (21)$$

Fig. 4b, d, f, and Table S4 summarize the results for MS coupons in acidic medium in presence and absence of **M1–M3** from 0.2 to 1.0 mM concentration at different temperatures. The positive enthalpy (ΔH) suggests that steel dissolution is endothermic shows the stronger interaction between the as-synthesized inhibitors and surface of MS strips. By adsorption onto the metal surface, inhibitors reduce the disorder and randomness of the system. Higher concentrations result in a more compact inhibitor layer, decreasing the entropy.[82] ΔH becomes less positive by increasing the inhibitor concentration. At higher concentration, the inhibitor molecules may occupy most of the available surface sites, leading to a decrease in the enthalpy change.[83] Moreover,

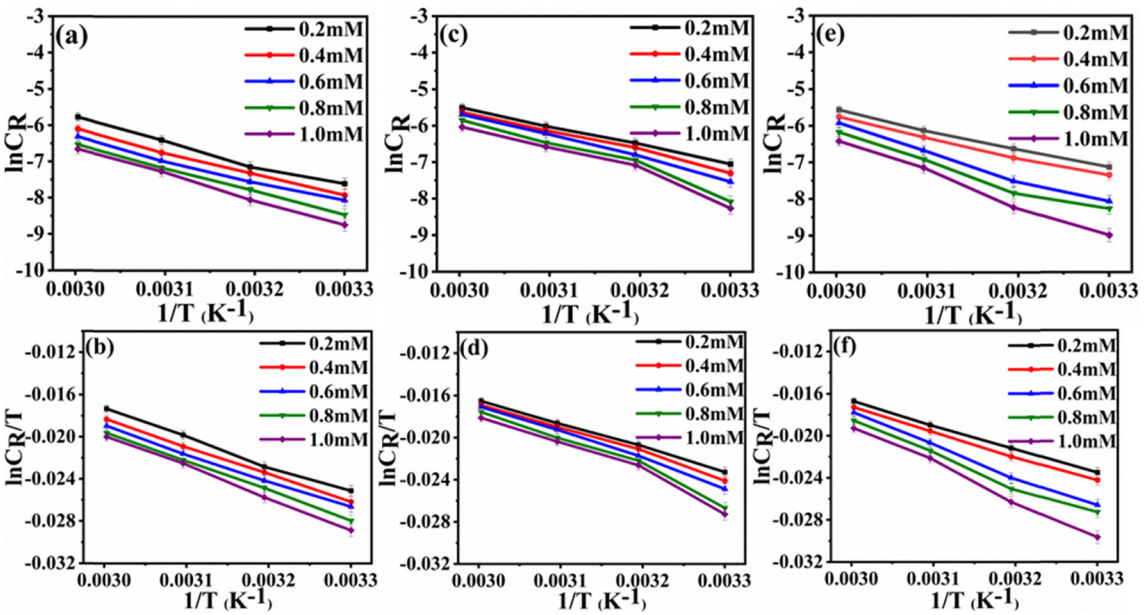

Fig. 4 Arrhenius (a), (c) and (e) and transition state (b), (d) and (f) plots for MS strips in acidic medium with and without **M1–M3** inhibitors (a) and (b) **M1**, (c) and (d) **M2** and (e) and (f) **M3**.

Table 2 ΔH (kJ mol^{-1}), and ΔS (kJ mol^{-1}) for MS coupons in acidic medium adsorbed by **M1–M3** with fitting parameters

Concentration (mM)	Slope	Intercept	R^2	ΔH (kJ mol^{-1})	ΔS (kJ mol^{-1})
M1					
0.2	−26.56 ± 1.2	0.0623 ± 0.004	0.99	220.80	−197.03
0.4	−26.24 ± 0.3	0.0604 ± 0.001	0.99	218.14	−197.04
0.6	−25.74 ± 0.8	0.0582 ± 0.002	0.99	214.05	−197.06
0.8	−24.55 ± 1.1	0.0538 ± 0.003	0.99	204.13	−197.10
1.0	−24.33 ± 1.0	0.0526 ± 0.003	0.99	202.30	−197.11
M2					
0.2	−27.16 ± 1.3	0.0655 ± 0.004	0.99	225.77	−197.00
0.4	−27.06 ± 0.5	0.0646 ± 0.002	0.99	224.98	−197.01
0.6	−26.71 ± 0.9	0.0628 ± 0.003	0.99	222.10	−197.02
0.8	−26.62 ± 1.0	0.0622 ± 0.003	0.99	221.28	−197.03
1.0	−25.98 ± 1.7	0.0596 ± 0.005	0.99	215.96	−197.05
M3					
0.2	−26.06 ± 0.8	0.0612 ± 0.002	0.99	216.63	−197.04
0.4	−25.69 ± 0.6	0.0590 ± 0.002	0.99	213.59	−197.06
0.6	−25.53 ± 1.0	0.0578 ± 0.003	0.99	212.24	−197.07
0.8	−25.44 ± 1.6	0.0571 ± 0.005	0.99	211.55	−197.07
1.0	−25.13 ± 1.8	0.0557 ± 0.006	0.98	208.89	−197.08

higher concentrations increase steric hindrance, reducing the enthalpy change.[84] ΔH of **M1** at 0.2 mM is 220.80 kJ mol^{-1}, which decreases to 202.30 kJ mol^{-1} (shown in Table 2) by increasing its concentration to 1.0 mM. Similarly, ΔH of **M2** decreases from 225.78 kJ mol^{-1} to 215.96 kJ mol^{-1} upon increasing concentration 0.2 to 1.0 mM. ΔH of **M3** is 216.63 kJ mol^{-1} and 208.89 kJ mol^{-1} for 0.2 and 1.0 mM concentrations, respectively. As the inhibitor concentration increases, the entropy decreases. This is due to a more structured arrangement, decreased randomness, development of a thick protective layer, and robust interactions between the inhibitor and the mild steel surface at elevated concentrations.[85] Entropy change (ΔS) of **M1** decreases −197.03 kJ mol^{-1} to −197.04 kJ mol^{-1} (shown in Table 2) as the concentration rises 0.2 to 1.0 mM. A similar trend is observed for **M2** and **M3**, with entropies of −197.00 kJ mol^{-1} and −197.04 kJ mol^{-1} at 0.2 mM, respectively, and −197.05 kJ mol^{-1} and −197.08 kJ mol^{-1} at 1.0 mM. The experimental data also compare the adsorption capabilities of **M1–M3** using thermodynamic parameters, specifically the enthalpy and entropy changes. These parameters decrease with increasing concentrations of **M1–M3**, indicating their strong interactions on the MS coupon surface. Experimental data suggest the lowest ΔH and ΔS for **M1** compared to **M2** and **M3** is attributed to the lowest steric hindrance caused by the adamantyl group on the electron rich heteroatoms N and O. But in cases of **M2** and **M3**, the heteroatoms feel more steric hindrance of the alkylated adamantyl groups on the electron donor heteroatoms reduces their adsorption capacity on the mild steel.

3.2.1.4. Adsorption isotherms. The adsorption equilibrium data were systematically studied by applying the Temkin, Freundlich, Flory–Huggins, and Langmuir isotherm models. A detailed comparison of the correlation coefficients (R^2) for all the models clearly establishes the superiority of the Langmuir model as shown in Table S11 and Fig. S34–S36. In the case of **M1**, the Langmuir model maintains high R^2 values at all temperatures, whereas the R^2 values for the Temkin model gradually reduce from 0.99 to 0.95. The R^2 values for the Freundlich model fluctuate between 0.96 and 0.98. The R^2 values for the Flory–Huggins model also show significant reductions at higher temperatures, as low as 0.91. In the case of **M2**, although the R^2 values for the Freundlich model are relatively higher at all temperatures, ranging from 0.97 to 0.98, the Langmuir model appears to be more reliable, as the R^2 values remain between 0.96 and 0.98 at all temperatures, whereas the R^2 values for the Temkin model are as low as between 0.88 and 0.95. For **M3**, the Langmuir model is again the best, as shown by the consistency of the R^2 values, ranging from 0.97 to 0.99, as opposed to the Freundlich model, whose consistency is slightly lower (0.95 to 0.99). The Temkin model, as before, is lower at 0.93 to 0.96. A more interesting observation is that the Flory–Huggins model shows a drastic drop in the R^2 value to 0.58 at higher temperatures, indicating its failure to properly describe the adsorption mechanism under such conditions. As observed, the Langmuir isotherm not only shows the best R^2 values but also shows the least variation with respect to temperature, indicating its superiority and reliability. Thus, it is highly indicative that the adsorption mechanism is best explained as one involving monolayer coverage on a homogeneous surface with energetically equivalent active sites and no significant intermolecular interaction, validating the Langmuir model as the best representation of the adsorption mechanism. The interaction between the surface if MS coupon and the inhibitor molecules were determined by calculating the surface coverage (θ) and Langmuir isotherms data fitting by using the eqn (22). C_{inh} represents the inhibitor concentration (mM) and K_{ads} is the equilibrium constant for adsorption process.[86]

$$\frac{C_{inh}}{\theta} = (K_{ads})^{-1} + C_{inh} \quad (22)$$

The graph plots between C_{inh}/θ and C_{inh} shown in Fig. 5 provides a straight line K_{ads} at different temperature (303–333 K) based on the inverse of intercept.

$$\Delta G^{\circ}_{ads} = -RT \ln(55.5 K_{ads}) \quad (23)$$

The ΔG°_{ads} easily calculated from eqn (23) by using the value of K_{ads}, the value 55.5 represents the [H_2O] in mol dm^{-3} adsorbed on the MS strip surface.

The negative values of ΔG°_{ads} for the compounds show spontaneous adsorption on the metal surface. The more negative values of Gibb's free energy favor the chemisorption. The Gibb's free energy value less than −20 kJ mol^{-1} represents physisorption adsorption mechanism.[87] In our study, **M1**, **M2** and **M3** shows −15.22 kJ mol^{-1}, −14.89 kJ mol^{-1} and −15.97 kJ mol^{-1} Gibb's free energies respectively at 303 K shown in Table 3. The values become less negative by increasing the temperature so the **M1**, **M2** and **M3** shows −13.68 kJ mol^{-1}, −10.72 kJ mol^{-1} and −13.18 kJ mol^{-1} Gibb's free energies respectively at 333 K. At low temperature, the Gibb's free energy data more likely to show chemisorption while high temperature favor the physisorption. Among the **M1–M3**, the **M1** shows comparatively more negative values than the **M2** and **M3** exhibits their more affinity to adsorbed

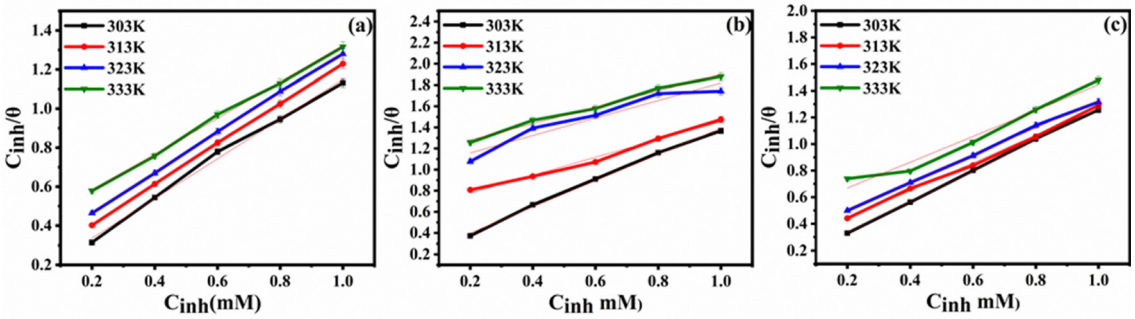

Fig. 5 Langmuir adsorption isotherms of inhibitors (**M1** (a), **M2** (b) and **M3** (c)) on the surface mild steel in 1.0 M HCl.

Table 3 K_{ads} and ΔG (kJ mol^{-1}) values for MS strips adsorbed by **M1–M3** with fitting data

Temperature (K)	Slope	Intercept	K_{ads}	R^2	ΔG (kJ mol^{-1})
M1					
303	1.018 ± 0.04	0.132 ± 0.13	7.57	0.99	−15.22
313	1.033 ± 0.01	0.199 ± 0.01	5.01	0.99	−14.65
323	1.025 ± 0.01	0.261 ± 0.01	3.82	0.99	−14.38
333	0.923 ± 0.02	0.396 ± 0.01	2.52	0.99	−13.68
M2					
303	1.242 ± 0.04	0.150 ± 0.03	6.66	0.96	−14.89
313	0.846 ± 0.05	0.609 ± 0.04	1.64	0.98	−11.74
323	0.827 ± 0.14	0.992 ± 0.09	1.01	0.93	−10.81
333	0.704 ± 0.08	1.153 ± 0.05	0.87	0.96	−10.72
M3					
303	1.167 ± 0.01	0.098 ± 0.01	10.21	0.99	−15.97
313	1.045 ± 0.03	0.231 ± 0.02	4.32	0.99	−14.26
323	1.033 ± 0.02	0.296 ± 0.01	3.38	0.99	−14.06
333	0.971 ± 0.10	0.474 ± 0.07	2.11	0.97	−13.18

on the surface of mild steel. This exceptional behavior of **M1** is explained by less steric hindrance by the adamantyl group on the electron donor N and O than the other inhibitors with more bulky adamantyl group.

Temperature variations in corrosion studies reveal the nature of adsorption of inhibitors on mild steel. Computed activation energy (E_a) for **M1**, **M2**, and **M3** lie in the range of ~44, 55 kJ mol^{-1} and are lower than the value of 80 kJ mol^{-1} which is considered as a signature of physisorption.[88] Therefore, it can be inferred that the adsorption of the inhibitors mainly occurs *via* a physisorption mechanism. Generally, physisorption features weak electrostatic interactions and is reflected by low activation energy values (E_a < 80 kJ mol^{-1}), whereas chemisorption is a result of strong coordinate bonding and is accompanied by elevated activation energies.[89] Additionally, the positive enthalpy values (ΔH) are an indication of the endothermic nature of the metal dissolution process. At the same time, the small decline in ΔH with raising inhibitor concentration shows a better interaction between inhibitor molecules and metal surface.[83] The negative entropy change values (ΔS) point out a loss of disorder in the activated complex formation, which is due to the regular adsorption of inhibitor molecules on the mild steel surface.[90] Although Gibbs free energy of adsorption (ΔG) values of around, 20 kJ mol^{-1} or less negative are generally related to electrostatic interactions, the ΔG values of adsorption (around, 10 to 16 kJ mol^{-1}) reported strengthen the case of physisorption being the major mechanism.[91] The presence of heteroatoms (N and O) that can donate electrons and the moderate magnitude of ΔG values suggest weak chemisorption contributions could have occurred. Hence, the overall adsorption mechanism may be regarded as a mixed-mode interaction where physisorption is the major one and chemisorption is the minor one. These observations are consistent with previously reported studies on organic corrosion inhibitors, where adsorption mechanisms often involve a combination of electrostatic interactions and partial charge transfer, especially in acidic media.[92] The reduction of the corrosion inhibition effectiveness as the temperature rises strongly indicates a physisorption-type mode of action, as physisorbed molecules are more likely to detach when exposed to higher temperatures.[93]

3.3. Electrochemical measurements

3.3.1. Open circuit potential (OCP) and Potentiodynamic polarization (PDP) measurements. The open circuit potential (OCP) were carried out between 0 to 1800s in presence and absence of inhibitors (**M1–M3**) in different concentration to verify that the inhibitors reached a stable potential.[94,95] The OCP ensure the equilibrium potential in the open circuit with no electrical interruption. This equilibrium forms between the interface of electrolyte and surface of electrodes. The OCP deviates in case of any interruption on the surface reaction. Fig. 6 and Table S6 represents the OCP curves of inhibitors different concentration of inhibitors and 1.0 M hydrochloric acid solution. All the OCP curves show that the inhibitors achieved the stable equilibrium potential in the concentrations of inhibitors and the results shows that the 800s is the sufficient waiting time for system to attain stable OCP curves. The blank 1.0 M HCl solution shows the OCP near −0.74 V while the OCP potential becomes least negative *i.e.* −0.54 V in case of 0.5 mM concentration of **M1** proves the higher concentration of inhibitors facilitate the surface electrochemical equilibrium due to presence of thick layer of inhibitors on the mild steel. The EIS and PDP measurements were performed after attaining the stable OCP curves in every experiment.

Potentiodynamic polarization (PDP) measurements were performed to determine the effect of different concentrations

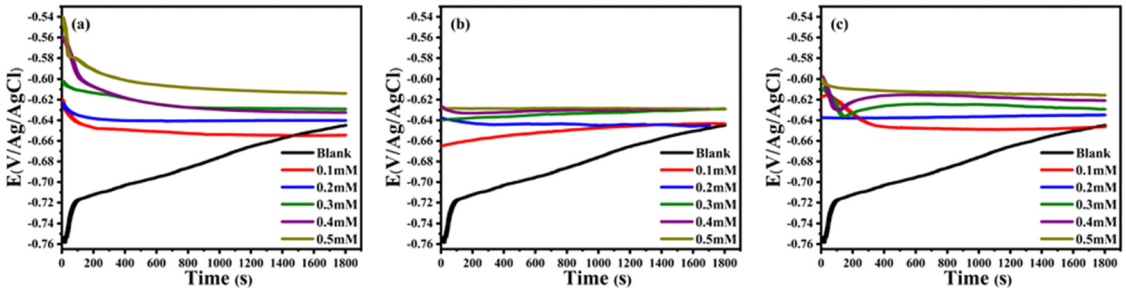

Fig. 6 OCP curves of MS coupons adsorbed by (a) **M1**, (b) **M2** and (c) **M3**.

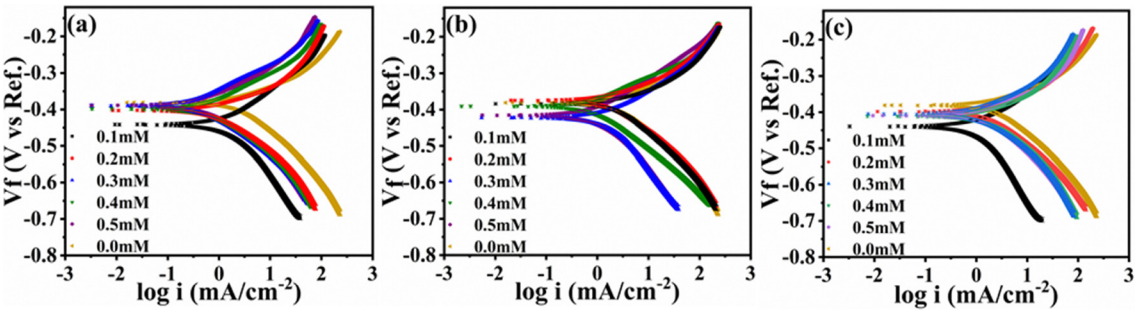

Fig. 7 PDP curves of MS coupons adsorbed by (a) **M1**, (b) **M2** and (c) **M3**.

of **M1–M3** on the corrosion inhibition process of MS strips in acidic medium. The corrosion current density (i_{corr}), anodic tafel curve (β_a), cathodic tafel curve (β_c) and corrosion potential (E_{corr}) obtained from PDP measurements. Furthermore, the IE% and polarization resistance (R_P) were determined by using the eqn (24) and (25) respectively, as follow:[96–98]

$$IE\% = \frac{i_{corr} - i_{inh}}{i_{corr}} \times 100 \quad (24)$$

$$R_P = \beta_a\beta_c/(2.303 \times i_{corr}) \quad (25)$$

The i_{corr} were calculated in mA cm^{-2} by extrapolating the tafel curves to the corrosion potential in presence and absence of the inhibitors. The PDP curves provides a visual representation of the corrosion behavior, were shown in Fig. 7 and Table 4, Table S7.

An effective anti-corrosion coating is characterized by reduced i_{corr} and an elevated E_{corr}.[99] When the mild steel is dipped in the solution of 1.0 M HCl, i_{corr} of 0.85 mA cm^{-2} and E_{corr} of −0.38 V were obtained. The i_{corr} and E_{corr} were decreased to 0.36 mA cm^{-2} and −0.44 V upon addition of 0.1 mM of **M1** in the acidic medium. The i_{corr} and E_{corr} of **M1** inhibitor shows 0.01 mA cm^{-2} and −0.40 V respectively by increasing the concentration to 0.5 mM. Similarly, the **M2** and **M3** exhibits i_{corr} of 0.60 mA cm^{-2} and 0.47 mA cm^{-2} respectively in 0.1 mM concentration. While the E_{corr} of **M2** and **M3** were −0.42 V and −0.44 V, respectively in 0.1 mM concentration. By increasing concentration of **M2** and **M3** up to 0.5 mM, the i_{corr} becomes less negative of −0.37 mA cm^{-2} and −0.38 mA cm^{-2} respectively. The E_{corr} of **M2** and **M3** at 0.5 mM concentration were decreased to 0.02 V and 0.04 V respectively.

Table 4 PDP parameters of MS coupons in presence and absence inhibitors (**M1–M3**)

Concentration (mM)	E_{corr} (V)	β_c (V dec^{-1})	β_a (V dec^{-1})	i_{corr} (mA cm^{-2})	R_P (Ω cm^{-2})	IE (%)
M1						
0	−0.38	0.12	0.20	0.85	0.01	0
0.1	−0.44	0.02	0.13	0.36	0.01	56.99
0.2	−0.41	0.08	0.10	0.33	0.04	60.41
0.3	−0.41	0.13	0.08	0.22	0.05	73.75
0.4	−0.41	0.13	0.06	0.03	0.06	96.63
0.5	−0.40	0.24	0.06	0.01	0.10	98.92
M2						
0.1	−0.42	0.14	0.11	0.60	0.01	29.02
0.2	−0.41	0.15	0.11	0.54	0.01	36.57
0.3	−0.39	0.16	0.09	0.46	0.01	45.08
0.4	−0.38	0.18	0.08	0.24	0.03	71.60
0.5	−0.37	0.19	0.08	0.02	0.42	98.22
M3						
0.1	−0.44	0.15	0.14	0.47	0.02	43.87
0.2	−0.40	0.16	0.13	0.43	0.02	49.66
0.3	−0.39	0.18	0.11	0.34	0.02	59.40
0.4	−0.38	0.19	0.11	0.25	0.03	70.44
0.5	−0.38	0.22	0.10	0.04	0.22	94.76

The findings also indicate that increasing the concentrations of inhibitors decrease the i_{corr} in anodic and cathodic tafel lines gives more promising effects at 0.5 mM concentration. This effect reduces the metal dissolution on anode, thereby demonstrating the efficiency of **M1–M3** as corrosion inhibitors. In **M1**, i_{corr} decreases 0.001 mA cm^{-2} while for **M2** and **M3**, i_{corr} decrease to 0.15 mA cm^{-2} and 0.04 mA cm^{-2}, respectively at 0.5 mM concentration. Similarly, E_{corr} increase to 0.40 V for **M2** and 0.42 V for **M3** at higher concentration of 0.5 mM. **M1** yields lower current density and higher voltage than **M2** and **M3**,

indicating that the **M1** effectively protects the iron coupons from corrosion.[100,101] Similarly, IE% of **M1–M3** also increases with increased concentrations (0.1–0.5 mM) as shown in Table 4. IE% of **M1** increases from 56.99 to 98.92 by increasing the concentration 0.1 to 0.5 mM. The IE% of **M2** increases from 29.02 to 98.22 and **M3** from 43.86 to 94.76, by raising the concentration from 0.1 to 0.5 mM. The polarization resistances (R_P) of **M1–M3** were also calculated by using the eqn (9) presented in Table 4. The R_P of mild steel in blank solution is 0.01 Ω cm^{-2}. The R_P values of **M1** increase 0.01 Ω cm^{-2} to 0.10 Ω cm^{-2} by enhancing the concentration from 0.1 to 0.5 mM, exhibits the anticorrosion potential improves with raising the concentration of inhibitors. The inhibitors **M2** (0.01 Ω cm^{-2} to 0.42 Ω cm^{-2}) and **M3** (0.02 Ω cm^{-2} to 0.22 Ω cm^{-2}) shows the same trend of increasing R_P with increasing concentration reveals their exceptional anticorrosion potential. **M1** inhibitor exhibits larger decrease in current density and increase in current voltage and IE% than the other inhibitors (**M2** and **M3**) because of less steric hindrance in its structure. In cases of **M2** and **M3**, the presence of more substituted alkyl groups decreases the electron-donating ability of heteroatoms due to steric hindrance.

3.3.2. Electrochemical impedance spectroscopy (EIS). EIS provides valuable information to deduce the corrosion mechanisms through the electrode and solution interface reactions. The bode, phase angle, and nyquist plots were generated during EIS measurements. The bode plot of the mild steel coating with a higher impedance value at low frequency shows maximum corrosion resistance.[102] In the case of phase angle, the coating exhibits a large absolute value of phase angle at the higher frequencies, with the platform showing maximum corrosion resistance.[103] The larger capacitor arc radius of the nyquist plot reveals better anti-corrosion properties.[99] Fig. 8a–c and 9a–f give the nyquist and bode plots that presents the impedance characteristics of MS coupon submerged in acidic medium, highlighting the influence of varying concentrations (0.1–0.5 mM) of inhibitors (**M1–M3**) on its corrosion behavior.

The nyquist plots (Fig. 8a–c and Table S8) of MS coupons in the blank acid solution give the minimum capacitor arc radius,

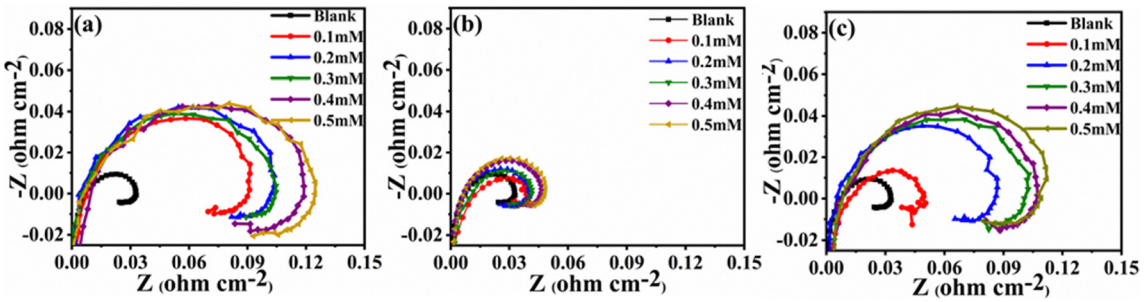

Fig. 8 Nyquist plots of MS coupons adsorbed by of inhibitors (a) **M1**, (b) **M2** and (c) **M3** in acidic medium.

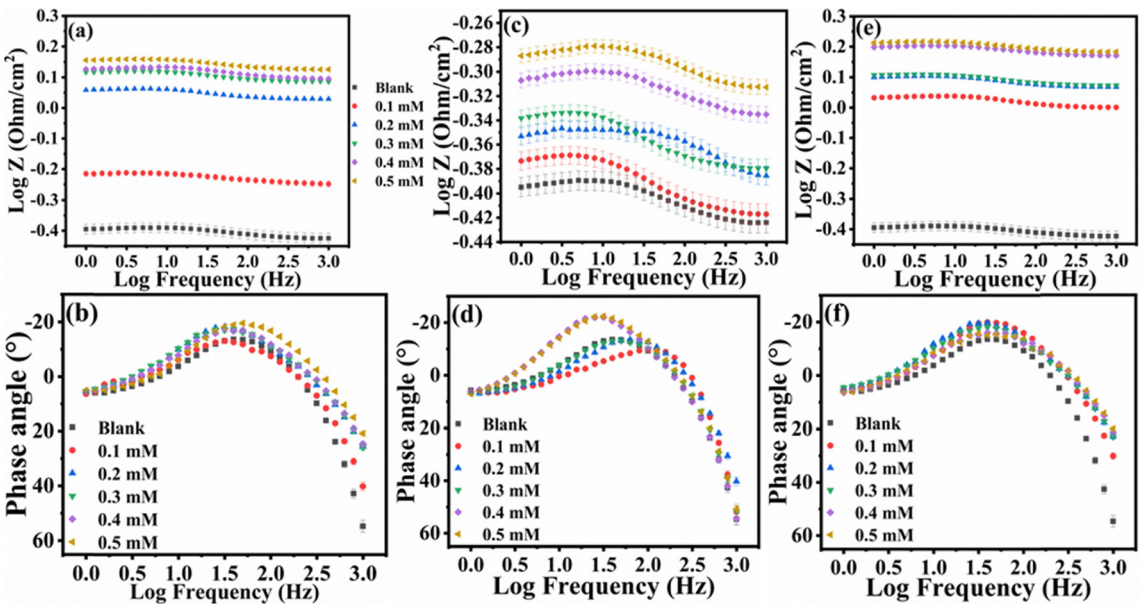

Fig. 9 Bode plots (a), (c) and (e) and phase angle plots (b), (d) and (f) of MS coupons adsorbed by organic inhibitors (**M1** = a, b, **M2** = c, d and **M3** = e, f) in acidic medium.

showing the maximum corrosion rate taken as reference for the inhibitors. The arc radius becomes wider in all the nyquist plots with increasing concentrations of the inhibitors, showing their anti-corrosion potential increase with concentration. All the inhibitors show maximum corrosion protection at higher concentration (0.5 mM). The maximum arc radius is observed in the **M1** showing the better anticorrosion performance of **M1** than **M2**, and **M3**.

Bode and phase angle plots at different concentrations (0.1–0.5 mM) of inhibitors (**M1–M3**) were shown in Fig. 9a–f and Table S9. All bode plots (**9a**, **9c**, **9e**) exhibit increase of impedance values with increase of concentration. All the inhibitors show highest value of impedance at low frequency. **M1** and **M3** show around 0.2 Ω cm^{-2} impedance (Z) at 0.01 Hz, while **M2** shows around −0.28 Ω cm^{-2} at 0.01 Hz. Higher impedance values at low frequency reveal effective anti-corrosion potential of inhibitors for mild steel. **M1** and **M3** show better anti-corrosion performance than **M2** due to higher impedance values at low frequency. On the other hand, the phase angle plots (**9b**, **9d**, and **9f**) move towards the positive at high frequency, elaborating the formation of effective protective layer of the inhibitors. The phase angle plots of the inhibitors presents a raised intensity in the phase angle curve with the raising the concentration of inhibitors. The maximum concentration of all the inhibitors shows that the capacitive rise of the phase angle curve indicates thicker protective layer formation on MS coupon surface. The shifting of phase angle towards the positive values at high frequencies for all inhibitors elaborates the improved corrosion protection. Among the inhibitors (**M1–M3**), **M2** shows the minimum impedance and capacitor arc radius in the nyquist plot, while lower impedance values are observed in the bode plot than for the other inhibitors. **M1** and **M3** exhibit the maximum impedance and maximum anti-corrosion properties in bode plot and a high capacitor arc radius. The **M1** and **M3** molecules could be adsorbed strongly on the MS coupons surface due to presence of lone pairs of heteroatoms in their structure are readily available for donation due to less steric hindrance in the structure, so they show the maximum anti-corrosion potential in the nyquist plot. On the other hand, **M2** has the maximum steric repulsion due to the presence of methyl groups on the adamantly fragment in its structure. The steric hindrance restricts the donor ability of lone pairs of heteroatoms, reducing the adsorption properties of **M2**, so it shows the minimum anti-corrosion tendency.

Fig. 10 shows the constant phase element (CPE) circuit used to resolve the impedance data, comprising a solution resistance (R_S) in series combined with polarization resistance (R_P) in parallel manner. Using this equivalent circuit, the impedance parameters, R_P and double layer capacitance (C_{dl}), were calculated by using eqn (26) as follow:

$$C_{dl} = \left(Y_0 {R_P}^{1-n}\right)^{1/n} \quad (26)$$

eqn (9) gives the C_{dl} based on the EIS data summarized in Table 5. This table includes the polarization resistance, denoted as R_P, both with and without the inhibitors (**M1–M3**). IE% increased due to enhancing the R_P at higher concentration of inhibitors indicates that effective adsorption on the surface

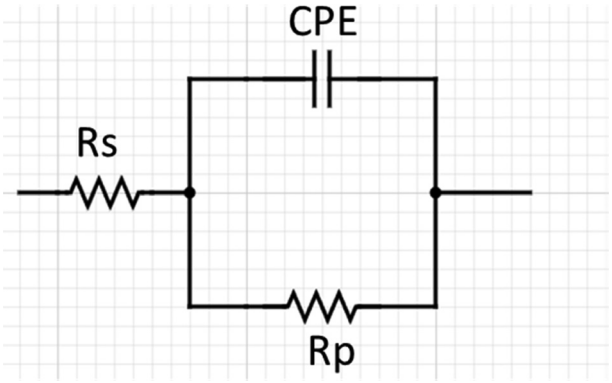

Fig. 10 Equivalent EIS circuit model.

of MS coupons.[104] The R_P values generated by EIS (shown in Table 5) and also determisned from tafel plots in PDP measurements (shown in Table 4) shows the same trend of increasing R_P values by increasing the concentration of the inhibitors reveals their reproducible and promising anticorrosion properties. The reduction C_{dl} could be explained by the formation of thick protective layer of inhibitors on metallic surface.[105] Collectively, these findings confirm that **M1–M3** form a barrier on the MS coupon surface, effectively resist from corrosive environment and significantly inhibiting the corrosion reaction, thus providing a robust protective mechanism.[106–108] In conclusion, the results summarized in Table 5 and Fig. 8, 9 show that the system without inhibitors has the maximum C_{dl} (100.29 μF cm^{-2}) and Y_0 (29.16 μS s^{α} cm^{-2}), while the systems with inhibitors show lower values of these factors, indicating the adsorption of inhibitors on the surface of mild steel. Furthermore, the decrease in Y_0 and C_{dl} with increasing inhibitor concentrations indicates a more effective protective layer formation on the steel surfaces. **M1** show 25.12 μF cm^{-2} C_{dl} at 0.2 mM which decreases to 18.11 μF cm^{-2} at 1.0 mM show promising anticorrosion activity at higher

Table 5 EIS parameters of MS coupon adsorbed by the inhibitors (**M1–M3**) in acidic medium

C_{inh} (mM)	R_S (Ω cm^{-2})	R_P (Ω cm^{-2})	C_{dl} (μF cm^{-2})	N	Y_0 (μS s^{α} cm^{-2})
M1					
0	0.02	0.38	100.29	1.27	29.17
0.1	0.02	0.58	25.12	1.53	6.82
0.2	0.03	1.08	25.11	1.53	6.08
0.3	0.06	1.23	25.11	1.53	6.05
0.4	0.06	1.26	25.05	1.54	5.45
0.5	0.08	1.38	18.11	1.50	5.03
M2					
0.1	0.01	0.40	28.24	1.24	27.67
0.2	0.01	0.43	27.60	1.30	25.13
0.3	0.01	0.43	27.36	1.32	21.36
0.4	0.02	0.48	24.92	1.54	21.30
0.5	0.02	0.50	25.34	1.52	8.71
M3					
0.1	0.01	0.50	27.75	1.29	24.81
0.2	0.01	00.50	27.73	1.29	24.37
0.3	0.06	1.01	27.93	1.27	21.21
0.4	0.07	1.18	25.11	1.52	7.25
0.5	0.07	1.20	25.12	1.53	7.22

concentration. Similarly, Y_0 decreases 6.82 μS s^{α} cm^{-2} to 5.03 μS s^{α} cm^{-2} by increasing the concentration 0.1 mM to 0.5 mM. C_{dl} of **M2** and **M3** at 0.2 mM are 28.24 μF cm^{-2} and 27.75 μF cm^{-2} while at 0.5 mM 25.34 μF cm^{-2} and 25.12 μF cm^{-2} respectively. Y_0 of **M2** and **M3** at 0.2 mM are 27.66 μS s^{α} cm^{-2} and 24.81 μS s^{α} cm^{-2} while at 0.5 mM 8.70 μS s^{α} cm^{-2} and 7.32 μS s^{α} cm^{-2} respectively. Among **M1–M3**, the **M1** inhibitor again shows the lowest values of C_{dl} (18.10 μF cm^{-2}) and Y_0 (5.03 μS s^{α} cm^{-2}) at high concentration (0.5 mM), indicating the largest anticorrosion potential. The less steric hindered structure of **M1** enables the binding ability of heteroatoms (O and N) in the structure to adsorb more effectively than the other inhibitors.

One should note that inhibition efficiencies (IE%) derived from weight-loss and electrochemical techniques, namely PDP and EIS, are usually not the same. That is quite a frequently mentioned phenomenon in corrosion researches as the sensitivity of the different methodologies and the exposure duration vary.[109] Weight-loss test gives the average corrosion rate over long immersion periods (up to 48 h), reflecting the whole material degradation.[40] On the other hand, electrochemical methods provide instantaneous corrosion rates after short stabilization time which is a kind of inhibitor performance at metal/solution interface. The higher IE% values gotten from electrochemical measurements compared to other methods might be explained by the fact that inhibitor molecules quickly adsorb and a protective film is formed during the first moments of immersion, which very effectively hinders the charge transfer reactions. Whereas, in weight-loss experiments where exposure time is very long, factors like small desorption of inhibitor molecules, surface heterogeneity, and destruction of the protective film over time, can somewhat decrease the average inhibition efficiencies. A similar variation between gravimetric and electrochemical methods for organic corrosion inhibitors has been very well documented in the literature.[1,44,110] Electrochemical methods, by their very nature, are more precise in detecting very minute interfacial processes like charge transfer resistance and double-layer capacitance. Conversely, weight-loss methods measure the whole material loss, which could also involve localized corrosion effects that electrochemical means might not be able to capture completely. Therefore, the differences seen in the IE% values by different methods are not only natural but also highlight the complementary nature of these methods in providing a comprehensive understanding of the corrosion inhibition effectiveness.[111,112]

Fig. 11 represents some reported compounds in literature derived from 4-aminoantipyrine with their IE% measured through electrochemical analysis. Govindaraju *et al.* report some Schiff bases derived from 4-aminoantipyrine (**AAP**) were 4-anisalidine amino antipyrine (**AAAP**), 4-benzalidine amino antipyrine (**BAAP**) and 4-salisilidine amino antipyrine (**SAAP**) undergoes PDP analysis shows promising anticorrosion potential. The IE% of 8.0 mM **AAP** was 82.48 in 1.0 M HCl solutions. In the **BAAP**, π electrons rich phenyl group was added to the **AAP** which increases the adsorption properties on the surface of mild steel and showed the IE% of 85.53. In cases of **SAAP** and **AAAP**, the PDP IE% were 90.83 and 87.40 due to presence of electron donor groups OCH_3 and OH respectively on the phenyl groups linked to the **AAP** through imine linkage. The electron donating OCH_3 and OH groups increases the electron density of at nitrogen of imine linkage and on benzene ring, increases their adsorption properties. On the other hand, Eldesoky *et al.* replaced the electron donating OCH_3 with electron withdrawing NO_2 group in case of 1,5-dimethyl-4-[(4-nitro benzylidene)-amino]-2-phenyl 1,2-dihydropyrazol-3-one (**C3**). The EIS data of NO_2 containing Schiff base of **AAP** show the IE% of 25.4 at 0.011 mM concentration in 2.0 M HCl. This abrupt decrease of adsorption ability of NO_2 group containing was due to electron withdrawing nature decreases the electron density of phenyl group and at imine linkage. Nnamdi C. Okey *et al.* reported a new Schiff base 4-[3-(4-methoxy-phenyl)-allylideneamino]-1,5-dimethyl-2-phenyl-1,2 dihydro-pyrazol-3-one (**TMCATP**) derived from 4-aminoantipyrine shows PDP IE% of 97.02 at 1.0 mM concentration in 1.0 M HCl. The **TMCATP**

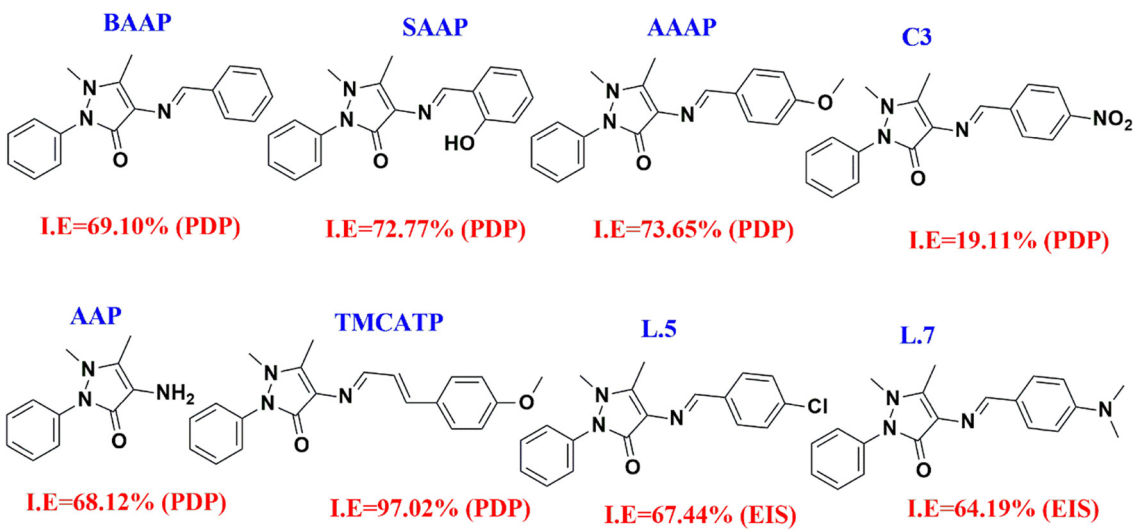

Fig. 11 Structure of 4-aminoantipyrine derivatives with their inhibition efficiencies.

contain the phenyl group attached with one double bond and methoxy group linked with 4-aminoantipyrine. This extended conjugation and electron donating effect methoxy group make the inhibitor more adsorptive on the surface of mild steel. Ankita *et al.* also reported (*E*)-4-((4-chlorobenzylidene)amino)-1,5-dimethyl-2-phenyl-1*H*-pyrazol-3(2*H*)-one (**L5**) and (*E*)-4-((4-(dimethylamino)-benzylidene)amino)-1,5-dimethyl-2-phenyl-1*H*-pyrazol-3(2*H*)-one (**L7**) derived from the 4-aminoantipyrine. The reported EIS IE% were 67.44 (**L5**) and 64.20 (**L7**) at 1.0 mM concentration in 1.0 N HCl. The **L5** bears the Cl group while **L7** have $N(CH_3)_2$ group on the phenyl ring attached with 4-aminoantipyrine. These electron donating groups were responsible for their large inhibition efficiencies.[113–117] In present study, the 4-aminoantipyrine (**AAP**) were linked with (electron donating groups) adamantyl and alkyl substituted adamantyl groups through two amide linkages containing O and N heteroatoms to enhanced their adsorption properties. The **M1** inhibitor give IE% of 98.92 while in case of **M2** and **M3** inhibitors gives the IE% of 98.22 and 94.76 at 0.5 mM concentration in 1.0 M HCl in PDP experiments. The highest PDP IE% values of **M1**, **M2** and **M3** than previous reported 4-aminoantipyrine derivatives reveal their promising anticorrosion potential.

Table 6 illustrates that the tested inhibitors match or even outperform in terms of inhibition efficiency those antipyrine derivatives already known in the literature, but at significantly lower concentrations. What is more, the design of the present compounds makes it possible to go beyond mere substituent effects when explaining their action mechanism, and this way it has been shown that functionalizing with adamantyl amide can enhance the corrosion inhibition by the joint effects of the hydrophobic film forming and the steric control of the adsorption-active donor atoms.

3.4. Surface analysis by SEM, EDX, FESEM and XPS

Fig. 12(a)–(d) represents the SEM images at 10 μm magnification power of MS coupons for 5.0 h of exposure to the 1.0 M HCl solution in presence and absence of 1 mM organic inhibitors (**M1–M3**). Fig. 12a illustrates the surface of MS coupons placed in blank acidic solution, clearly shows the severe corrosion with a highly porous, rough, and cracked structure. However, the surface of MS coupons exposed to acidic medium along with organic inhibitors **M1**, **M2**, and **M3**, as shown in Fig. 12b–d became smooth, less porous, less cracked, and rigid due to the formation of a thick layer by as-synthesized inhibitors (**M1–M3**). The compact layer of organic inhibitors protects the MS coupons from corrosion in an extremely acidic solution. Fig. 12b shows that the **M1** forms a more dense layer compared to **M2** (Fig. 12c) and **M3** (Fig. 12d). The formation of a dense layer by the **M1** was due to the less steric hindrance in the structure, which may provide more donating ability to form a more stable structure. These SEM results are similar to the outcomes of weight loss and electrochemical studies.

Fig. 13(a)–(c) and Table 7 elaborates the results of EDX analysis performed on the MS strips exposed in 1.0 mM/1.0 M HCl solutions of inhibitors **M1** (13a), **M2** (13b) and **M3** (13c). The **M1** inhibitor adsorbed on the MS strip **M1** inhibitor shows the atomic percentage compositions of carbon 35.18, nitrogen 1.70, oxygen 6.29 and iron 39.04. On the other hand the MS strips of **M2** show carbon 37.90, nitrogen 1.86, oxygen 18.76 and iron 25.09 and the **M3** have carbon 52.90, nitrogen 1.59, oxygen 33.73 and iron 2.43.

All the EDX spectra clearly show the peaks of heteroatoms (nitrogen and oxygen) along with the carbon in sufficient proportion indicates the successful adsorption of inhibitors on the surface of mild steel coupons through heteroatoms and act as strong anticorrosion protective layer.

The surface of best performing inhibitor **M1** was also analyzed by the FESEM shown in Fig. 14.

The FESEM images were taken in different magnification (14a at 20 μm, 14b at 10 μm, 14c at 2 μm and 14d at 500 nm). All the FESEM images show the complete surface coverage, minimum cracks and strong adsorption of **M1** on the MS surface to protect it completely from corrosion.

XPS analysis was performed on the MS coupon exposed in acidic medium with 1 mM **M1** (Best performing inhibitor) for 5.0 h immersion time. The XPS survey peaks confirms the adsorption of **M1** on the MS surface by exhibiting the presence of C 1s, O 1s, N 1s, Fe 2p, C KLL, N KLL, O KLL, Cu 2p, Al 1s, KLL and Al 1s peak as shown in Fig. 15a. The surveys graph includes the peaks of heteroatoms (O and N) reveals the adsorption of inhibitor.

The deconvolutions of high resolution XPS peaks present the well-defined results to understand the adsorption mechanism shown in Fig. 15b–f and Table 8. The deconvoluted high resolution graph of C 1s generates the 3 peaks with binding energies 288.1 eV, 288.8 eV and 289.9 eV which confirms the

Table 6 Comparison of previously reported 4-aminoantipyrine-based corrosion inhibitors with the present adamantyl amide derivatives

Inhibitor	Structure type	Medium	Method	Conc. (mM)	IE (%)	Mechanistic insight	Ref.
AAP	Parent antipyrine	1.0 M HCl	PDP	8.0	82.48	Baseline adsorption	113 and 114
BAAP	Schiff base (phenyl)	1.0 M HCl	PDP	8.0	85.53	π-conjugation enhances adsorption	113 and 118
SAAP	Schiff base (OH)	1.0 M HCl	PDP	8.0	90.83	Electron-donating substituent	113
AAAP	Schiff base (OCH_3)	1.0 M HCl	PDP	8.0	87.40	Electron-donating aromatic group	113 and 114
C3	NO_2-Schiff base	2.0 M HCl	EIS	0.011	25.4	Electron-withdrawing reduces adsorption	114
TMCATP	Extended conjugation	1.0 M HCl	PDP	1.0	97.02	Conjugation + donation	115
L5	Schiff base (Cl)	1.0 N HCl	EIS	1.0	67.44	Substituent effect	13
L7	Schiff base ($N(CH_3)_2$)	1.0 N HCl	EIS	1.0	64.20	Limited donor efficiency	13
M1	Adamantyl amide	1.0 M HCl	PDP	0.5	98.92	Hydrophobic + low steric hindrance	This work
M2	Substituted adamantyl	1.0 M HCl	PDP	0.5	98.22	Steric hindrance reduces activity	This work
M3	Bulky amide derivative	1.0 M HCl	PDP	0.5	94.76	Hydrophobic but hindered adsorption	This work

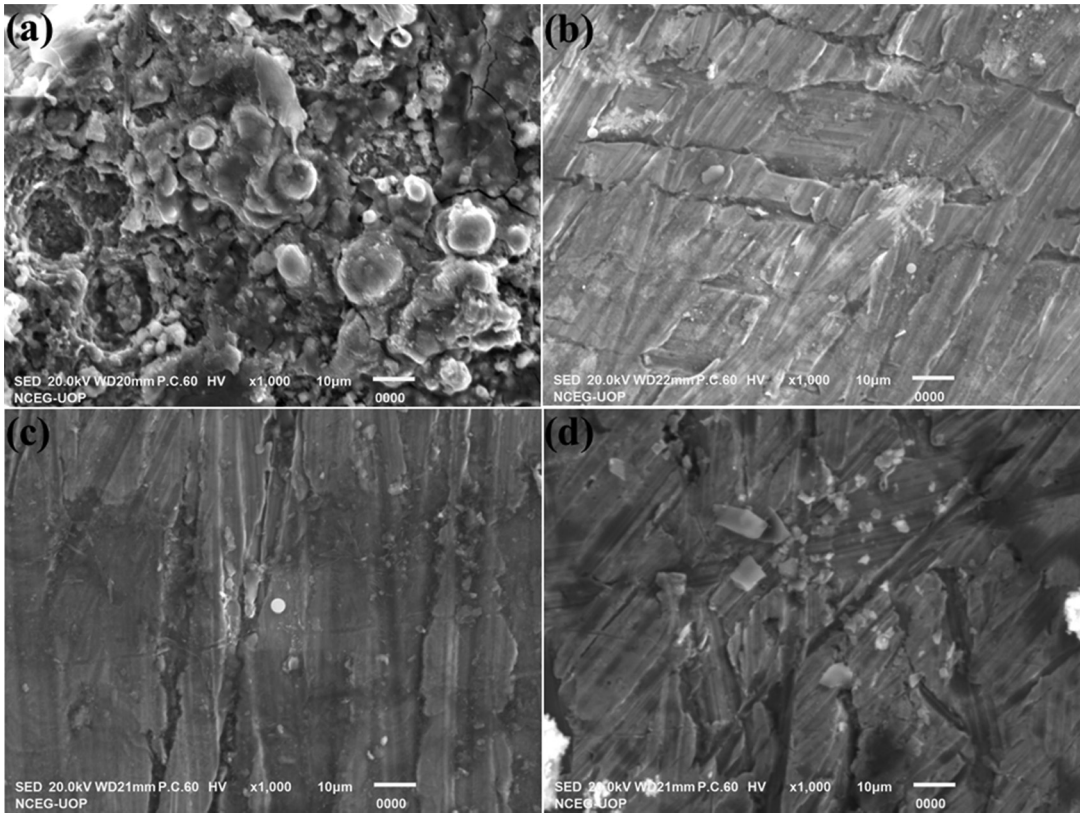

Fig. 12 SEM micrographs of mild steel coupon immersed (a) 1.0 M HCl blank, (b) **M1**, (c) **M2** and (d) **M3** for 5.0 h immersion time at 1 mM concentration in 1.0 M HCl.

metallic surface bears C–O, C–N, C═O, O–C–O and O–C═O groups.[119,120] The deconvoluted high resolution graph of N 1s exhibits two XPS strong peaks with binding energies 400.7 eV and 401.2 eV. The peaks confirm the presence of amidic nitrogen, pyrazolone ring nitrogen, protonated amide and Fe–N groups on Mild steel surface.[121] The high resolution graph of O 1s deconvoluted to produce peaks at 527.95 eV, 530.6 eV, 531.7 eV and 532.2 eV. These peaks correspond to OH, Fe–O, C═O, H_2O Oxygen of **M1** and chemisorbed oxygen on the MS surface.[122] The deconvoluted high resolution spectra also covers the Fe 2p region and gives peak at 709.5 eV, 711.1 eV and 724.6 eV. These peaks show the presence of Fe, Fe_2O_3, Fe(II), Fe(III), Fe_3O_4 and Fe–O on the MS steel strips.[123] In conclusion the thermodynamic and different surface analysis supports physioorption and chemisorption of inhibitors on the MS surface. The heteroatoms (N and O) and carbon chains present on inhibitor structure play vital rule for adsorption on metallic surface and shows exceptional corrosion inhibition efficiency. All the results of XPS analysis are shown in Fig. 15a–f in the form of survey and high resolution graphs. The binding energies (eV) data and predicted assignments are summarized in Table 8.

3.5. DFT calculations

3.5.1. Frontier molecular orbitals (FMO), Mulliken charges and global reactivity descriptors. The geometrical shapes of the as-synthesized inhibitors were refined at the B3LYP/def2-SVP level of theory. To confirm the all refined geometries have no negative frequency and minimum potential energy surface, the harmonic frequency calculations were used at the same level. Upon the refined geometries gained, the Mullikan charges of inhibitors were determined and the frontier molecule orbitals, FMOs, HOMO and LUMO were calculated directly. Fig. 16 shows 3D refined geometries and special configuration of the HOMO and LUMO spread over the structure of the as-synthesized organic inhibitors.

Mullikan charges are often used to identify the special centers of molecules which have ability to adsorbed.[124] The Mullikan charges calculated are given in Table 9, showing that the heteroatoms (oxygen and nitrogen) of the molecules have the maximum negative charge justifying their ability to donate electrons for adsorption on the metallic surface. The nitrogen and oxygen along with some carbons in the structure contain maximum negative charge could be perfect sites for making interaction on to the metallic surface due of their greater electron density. Moreover, the presence of the aryl group favors adsorbate-surface complex formation.[125] Mulliken charge distribution analysis provides the significant information regarding the adsorption behavior of the tested inhibitors (**M1**, **M2**, and **M3**) as shown in Table 9. A detailed comparison of the important charge values for the molecules indicates that these molecules are characterized by multiple electron-rich heteroatoms (N and O) that act as the main adsorption centers for the molecules, interacting with the vacant d-orbital of iron of mild steel through donor–acceptor interactions. In **M1**, the nitrogen atoms are characterized by

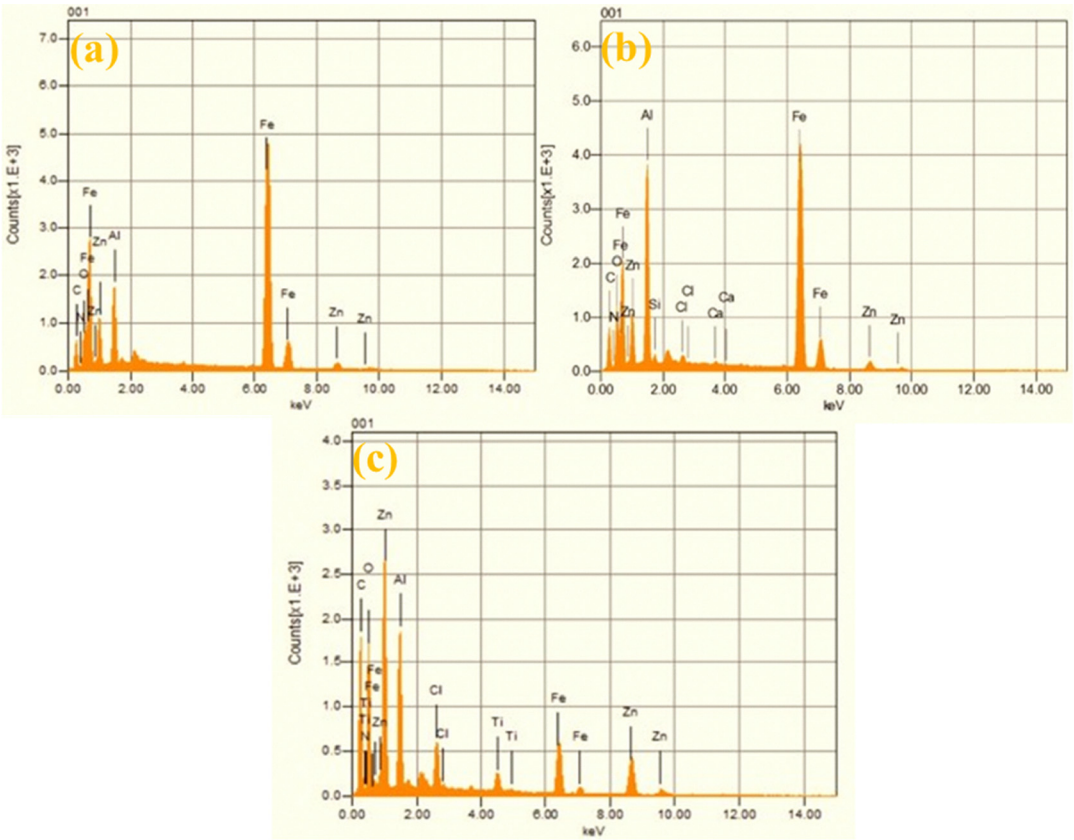

Fig. 13 EDX spectra of (a) **M1**, (b) **M2**, and (c) **M3** after 5.0 h immersion time in acidic medium.

Table 7 Results of EDX analyses of MS coupon surface adsorbed by inhibitors (**M1–M3**) in acidic medium

	Percentage atomic composition		
Elements (symbol)	**M1**	**M2**	**M3**
C	35.18	37.90	52.90
N	1.70	1.86	1.59
O	12.68	18.76	33.73
Fe	39.04	25.09	2.43

significant negative charge values, *i.e.*, N1 = −0.1679, N10 = −0.1153, while the oxygen atoms, *i.e.*, O21 = −0.2633 and O22 = −0.2669, also have significant electron density, thus showing high electron-donating ability. On the contrary, **M2** has comparatively less favorable characteristics, whereby, although the oxygen atoms possess a substantial negative charge (O24 ≈ −0.2680, O26 ≈ −0.2785), the replacement of adsorption centers by positively charged carbon atoms (C25 ≈ +0.1573) and a reduction in the electron density of the nitrogen atoms (N1 ≈ −0.1703, N27 ≈ −0.1412) could compromise its adsorption capability on the metal surface. Furthermore, **M3** has intermediate adsorption characteristics, whereby highly negative charges on the oxygen atoms (O21 ≈ −0.2985, O24 ≈ −0.2763) indicate a substantial localized electron density, although a relatively lower contribution from the nitrogen atoms (N1 ≈ −0.1625, N10 ≈ −0.0968) and a non-uniform distribution of charges compromise its adsorption capability relative to **M1**. Furthermore, the presence of positively polarized carbon atoms in all the adsorbate molecules (C23 ≈ +0.1629, **M1**; +0.1573, **M2**; +0.1640, **M3**) facilitates electrostatic interactions with the metal surface, thereby confirming a mixed adsorption process that combines chemisorption and physisorption mechanisms. This is supported by theoretical principles that a higher negative charge density on the heteroatoms improves adsorption and inhibition efficiency.[6,126–128] The 3D optimized structure of the molecules **M1**, **M2** and **M3** with atoms numbers are given in Fig. S33 (SI). The electronic structure analysis of the synthesized molecules **M1**, **M2**, and **M3** revealed distinct variations in their frontier orbital energies and band gaps, both in neutral and protonated states (Fig. 16(a) and (b)).

The E_{HOMO} value of a molecule is indicative of its electron-donating ability, with higher E_{HOMO} values indicating easier donation of electrons to acceptor molecules with low energy, empty molecular orbitals. The E_{LUMO} value, on the other hand, represents the ability of molecule to accept electrons, with lower E_{LUMO} values indicating greater ease of electron acceptance. The absolute hardness (η) reflects the stability of a compound, while the global softness (S) quantifies the electron cloud polarization and is the opposite of hardness. A higher energy gap (ΔE_{gap}) indicates lower polarity, making the adsorption of the molecule on a metal surface more challenging. An effective corrosion inhibitor typically exhibits low ΔE and η values but a high S value. The calculated quantum chemical parameters from FMOs

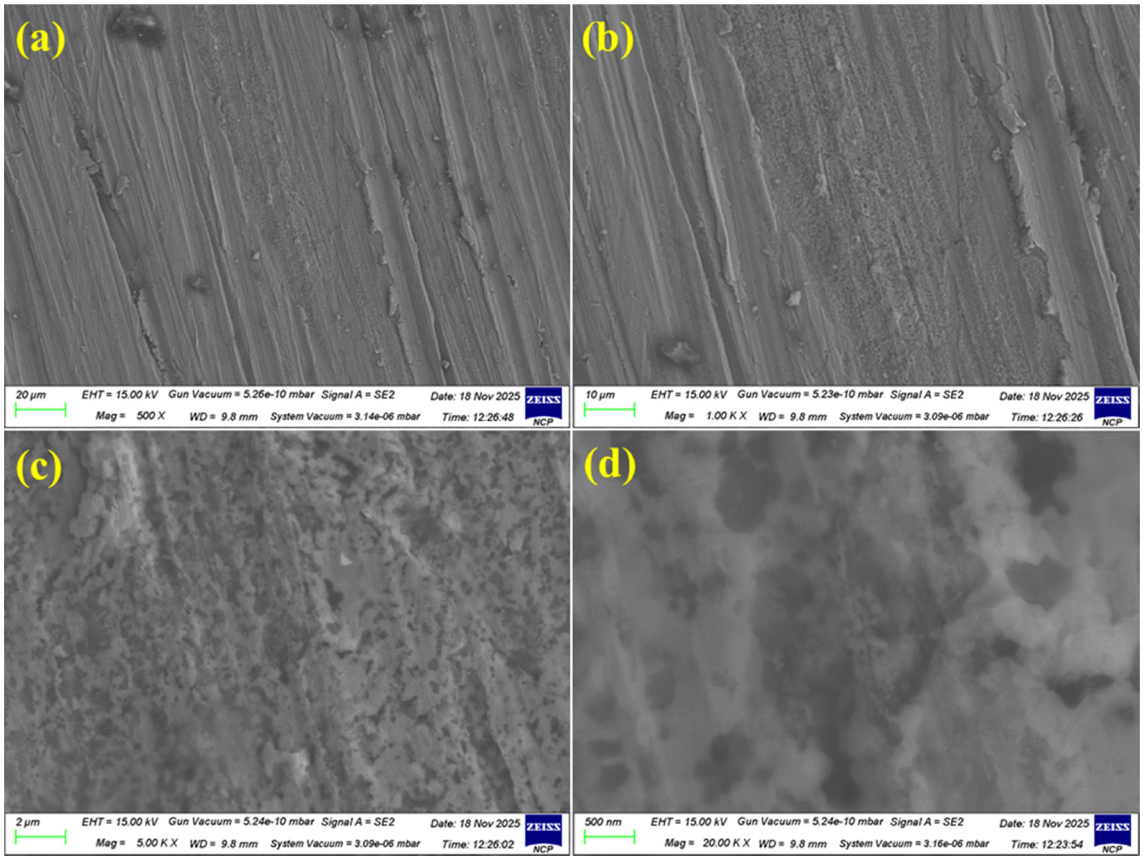

Fig. 14 FESEM images of **M1** inhibitor at magnification power of (a) 20 μm, (b) 10 μm, (c) 2 μm and (d) 500 nm after 5 hours immersion time at 1 mM concentration in 1.0 M HCl.

for the molecules (**M1**, **M2** and **M3**) both in neutral and protonated states are given in Table 10. According to the values in Table 10, all molecules (**M1**, **M2** and **M3**) demonstrate excellent corrosion inhibition properties, as their calculated quantum chemical parameters. In the neutral Form, **M1** showed the highest value of E_{HOMO} (−5.042 eV) and the smallest energy gap (ΔE_{gap} = 4.321 eV) in comparison to **M2** and **M3**. The high value of E_{HOMO} indicates a better ability of the molecule to donate electrons to the vacant d orbitals of the metal surface, thus forming a coordinate bond. With protonation, major changes in the electronic configuration were observed. The values of E_{HOMO} for all the inhibitors decreased, indicating a more negative value. However, the trend for E_{HOMO} was similar to that in the neutral state. The energy gap ΔE_{gap} is a major criterion for chemical reactivity and kinetic stability. In both the neutral and protonated states, the values of ΔE_{gap} for all three inhibitors are in the order **M1** < **M3** < **M2**. The energy gap for **M1** is lower, indicating higher molecular reactivity and lower excitation energy, thus increasing the adsorption potential on the mild steel surface. On the other hand, **M2** showed a higher energy gap in both states, indicating higher kinetic stability and a lower adsorption potential. The general notion is that the greater the dipole moment, the greater its ability to have protective action upon the metal surface. As shown from the computed results (Table 11), the dipole moment of the inhibitors studied were observed to be larger than that of the water molecule (μ = 1.84 Debye). The results provided suggest that the adsorption process of the studied inhibitors can be compared with that of replacing water on the metal surface while in solution. The vertical ionization potential I_v is defined as the amount of energy needed to remove an electron. The least I_v is observed for the neutral state of **M1** (5.151 eV). Hence, it is the most capable of donating electrons to the metal. However, after protonation, the I_v of all the molecules is high (6.769 eV for **M2**). Hence, it is clear that after protonation, it is more difficult to remove electrons because the electrons are more stable. On the other hand, the electron affinity A_v is defined as the amount of energy that is required to add an electron to the molecule. The highest A_v is observed for the neutral state of **M1** as compared to other molecules **M2** and **M3**. The increase in A_v in protonation form (1.523 eV for **M2** and **M3**) shows that it is easier for the protonated molecules to accept electrons from the metal. The electronegativity (χ) of the molecule represents the ability of the molecule to attract electrons towards itself. The neutral **M3** has the highest electronegativity of 3.088 eV. It represents the ability of the molecule to pull electrons towards itself. The chemical potential (Π) of the molecule represents the negative of electronegativity. The more negative the chemical potential of the protonated molecules, the more stable the electronic system of the molecules, although highly reactive at the metal interface.

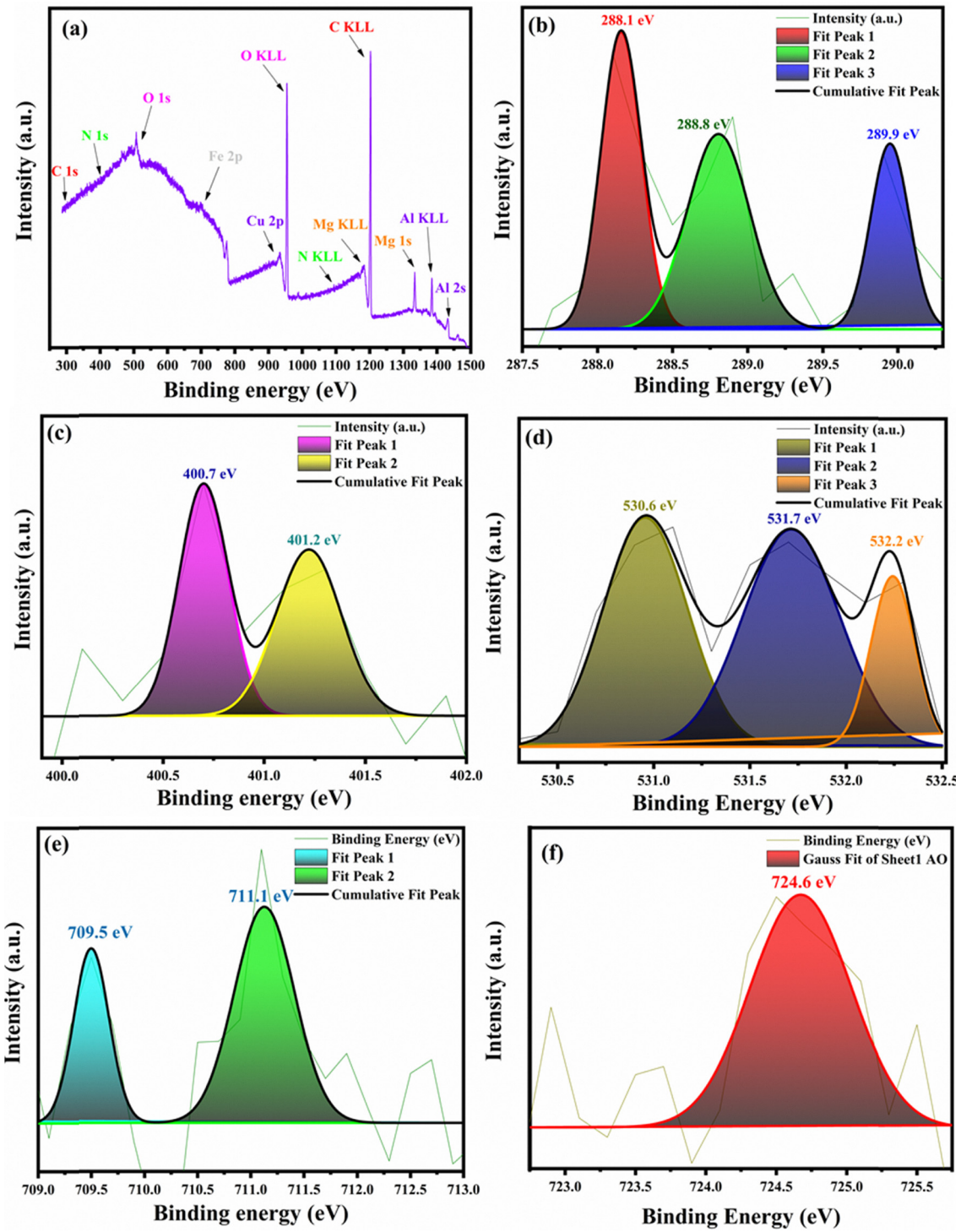

Fig. 15 XPS surface analysis: (a) the XPS survey spectrum and the XPS spectrum of (b) C 1s, (c) N 1s, (d) O 1s, (e) Fe $2p_{3/2}$, (f) Fe $2p_{1/2}$ immersed in 1 M HCl containing 1 mM **M1** inhibitor.

According to the HSAB theory, a ''soft'' inhibitor is more efficient because it more readily interacts with ''soft'' iron atoms on the metal surface. **M1** and **M3** are ''softer'' in their neutral state compared to **M2**. The lower value of hardness and higher value of softness (S) for **M1** indicate that its cloud is more easily polarizable, thus showing easier transition during the adsorption process on mild steel. The electrophilicity index (ω) is a measure of the total electrophilic nature of the molecule. From the results, it can be observed that the electrophilicity index increases upon protonation of the molecule. This indicates that the inhibitors possess a higher electrophilic nature in the acidic medium and can accept the electron density from the d-orbitals

Table 8 XPS results corresponding to the **M1** layer adsorbed onto the steel surface after 5 hours immersed in 1.0 M HCl

Element	Binding energy (eV)	Assignment
C 1s (13b)	288.1	C–O, C–N
	288.8	C–N, C═O, O–C–O
	289.9	O–C═O
N 1s (13c)	400.7	Amide, NH_2
	401.2	$CONH_2$, protonated amide
O 1s (13d)	530.6	OH, metal oxides
	531.7	OH, C═O
	532.2	C═O, H_2O
Fe $2p_{3/2}$ (13e)	709.5	Fe(0), Fe(II), Fe_2O_3
	711.1	Fe(III), Fe_3O_4
Fe $2p_{1/2}$ (13f)	724.6	Fe(III), Fe_3O_4

of the metal, thereby stabilizing the protective. Finally, the calculation of number of electron transfers calculated by the DFT studies shows the **M1** highest ΔN value compared to **M2** and **M3**, indicating that the **M1** has more ability of the electron donation to make interaction with the mild steel surfaces. Hence, **M1** is expected to possess the highest inhibition efficiency because it is better at donating electrons to the mild steel surface. Inspection of Table 10 shows that the $\Delta E_{b\text{-}d}$ derived for the **M1**, **M2** and **M3** inhibitors are <0 indicating that transfer of electron density to a molecule followed by back donation of electron density from the molecule to the Fe-surface is energetically favored situation. The negative values and small deviation between the $\Delta E_{b\text{-}d}$ values for the molecules simply confirms that these inhibitors behave like good corrosion inhibitors. Studies showed that there is a better relationship between inhibitor polarity and inhibitive ability.[129] In conclusion, from the above results, we can see that for the three molecules (**M1**, **M2**, and **M3**) that we studied, they all exhibit the inhibition ability to protect the Fe surface with **M1**, on very slight preference over **M2** and **M3**. The mechanism of interaction, which involves predominantly chemisorption on a metal surface (soft-center), is well described by the principles of chemical softness and electron transfer.

In order to give a quantitative evidence to the correlation of frontier molecular orbital (FMO) descriptors with the experimental inhibition efficiency (IE%), a regression analysis was carried out using main quantum chemical parameters. Out of the explored descriptors, the fraction of electron transfer (ΔN) showed the highest positive correlation with experimentally obtained IE% values, giving the coefficient of determination ($R^2 \approx 0.79$) shown in Table 11. In this relation the IE% of **M1**, **M2** and **M3** from electrochemical analysis of 98.92, 98.22 and 94.70 respectively related with their ΔN values of 0.95, 0.92 and 0.90 with good R^2 of 0.79. This high correlation means that the capability of the inhibitor molecules to donate electrons is the most important factor for their adsorption on the mild steel surface and, therefore, their corrosion inhibition enhancement. Especially, the higher ΔN value of **M1** is well in line with its better inhibition efficiency, whereas **M2** and **M3** come at the next steps. In contrast, other descriptors such as the energy gap (ΔE_{gap}) and global softness (S) showed relatively weak correlations with IE%

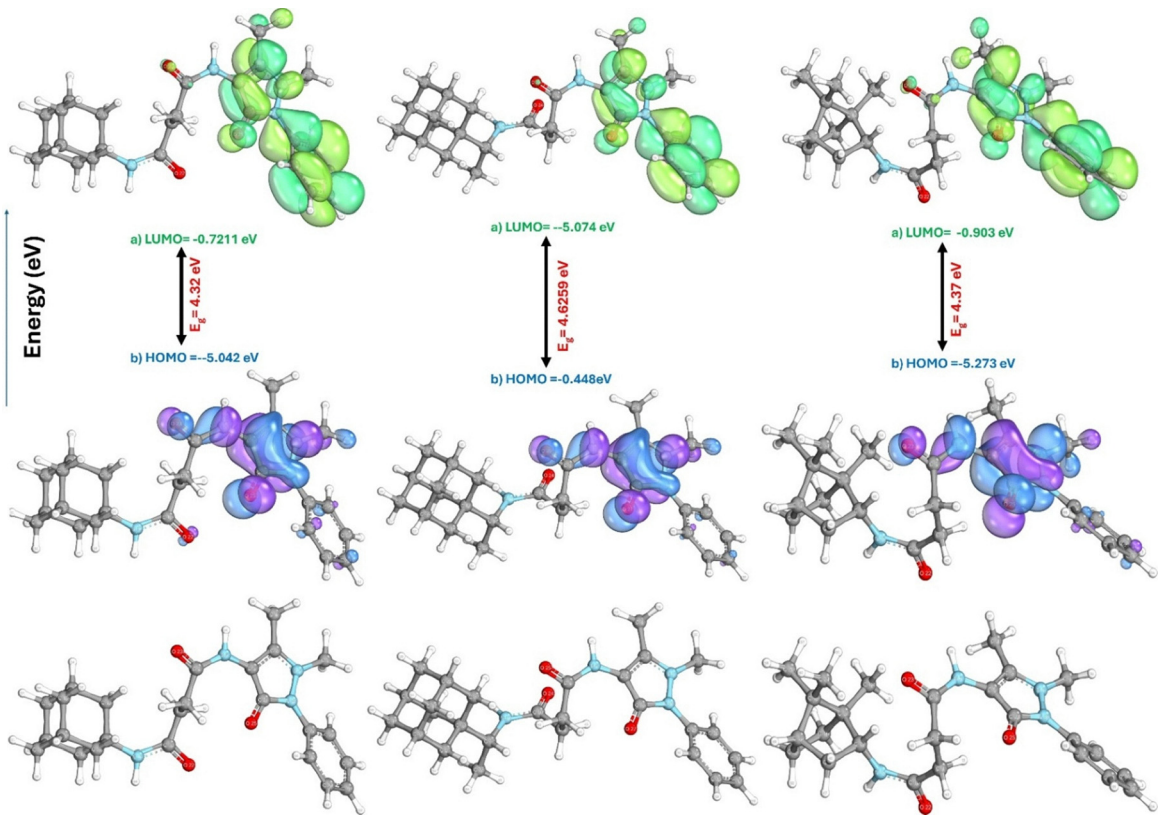

Fig. 16 HOMO (blue), and LUMO (green) energy levels and optimized 3D structures (bottom) of the synthesized molecules **M1**, **M2** and **M3**.

Table 9 Mullikan charges for synthesized molecules (**M1**, **M2**, **M3**)

M1						**M2**						**M3**					
Atom	Charge	Atom	Charge	Atom	Charge	Atom	Charge	Atom	Charge	Atom	Charge	Atom	Charge	Atom	Charge	Atom	Charge
0 C	0.1159	24 O	−0.2625	48 H	−0.0148	0 C	0.122954	24 O	−0.26801	48 H	−0.01926	0 C	0.120314	24 O	−0.27629	48 H	−0.01503
1 N	−0.1679	25 N	−0.1448	49 H	−0.0129	1 N	−0.17034	25 C	0.157261	49 H	−0.01497	1 N	−0.16247	25 N	−0.14298	49 H	−0.01525
2 C	−0.0439	26 C	0.21693	50 H	−0.0152	2 C	−0.03636	26 O	−0.27852	50 H	−0.01557	2 C	−0.02003	26 C	0.203604	50 H	−0.01827
3 C	0.08376	27 C	−0.0388	51 H	−0.0164	3 C	0.092286	27 N	−0.14119	51 H	−0.01852	3 C	0.046717	27 C	−0.02954	51 H	−0.01124
4 C	−0.061	28 C	0.02137	52 H	−0.0194	4 C	−0.04844	28 C	0.20744	52 H	−0.01456	4 C	−0.06917	28 C	0.012986	52 H	−0.00159
5 N	−0.0701	29 C	0.03458	53 H	−0.0047	5 N	−0.06542	29 C	−0.03062	53 H	−0.01996	5 N	−0.06572	29 C	0.038738	53 H	0.01452
6 C	0.04384	30 C	0.01454	54 H	−0.0142	6 C	0.041079	30 C	0.014636	54 H	−0.01536	6 C	0.05335	30 C	0.012233	54 H	−0.01203
7 C	0.04802	31 C	0.01577	55 H	0.00196	7 C	0.094719	31 C	0.03423	55 H	−0.02094	7 C	0.076392	31 C	0.011939	55 H	−0.00321
8 C	0.05165	32 H	0.03983	56 H	−0.0143	8 C	0.030205	32 C	0.015239	56 H	−0.01814	8 C	−0.00783	32 H	0.044217	56 H	0.003726
9 C	0.03555	33 H	0.0541	57 H	−0.0211	9 C	0.039754	33 C	0.004984	57 H	−0.02029	9 C	0.054081	33 H	0.054159	57 H	0.003789
10 N	−0.1153	34 H	0.05971	58 H	0.00143	10 N	−0.14476	34 H	0.037432	58 H	−0.0136	10 N	−0.09677	34 H	0.059248	58 H	0.019002
11 C	−0.1557	35 H	0.04214	59 H	−0.0581	11 C	0.096832	35 H	0.053574	59 H	−0.00829	11 C	0.05408	35 H	0.015638	59 H	−0.00762
12 C	0.10851	36 H	0.04346	60 H	−0.0217	12 C	−0.25322	36 H	0.056611	60 H	0.004716	12 C	0.177899	36 H	0.050453	60 H	0.014151
13 C	0.12314	37 H	0.01896	61 H	−0.0213	13 C	0.104773	37 H	0.044861	61 H	0.003326	13 C	−0.05867	37 H	0.059907	61 H	−0.05112
14 C	−0.0934	38 H	0.12242	62 H	−0.0126	14 C	0.117646	38 H	0.038521	62 H	0.009516	14 C	0.101432	38 H	0.126413	62 H	−0.01684
15 C	0.10377	39 H	0.00568	63 H	−0.0005	15 C	−0.07806	39 H	0.023916	63 H	0.013068	15 C	0.08147	39 H	0.005176	63 H	−0.01817
16 C	0.12421	40 H	0.05345			16 C	0.10302	40 H	0.123097	64 H	0.00705	16 C	−0.21486	40 H	0.043934	64 H	−0.0108
17 C	−0.1026	41 H	0.01691			17 C	0.105322	41 H	−0.0164	65 H	−0.05646	17 C	0.103589	41 H	0.041144	65 H	−0.00139
18 C	0.10387	42 H	−0.0026			18 C	−0.08145	42 H	0.044735	66 H	−0.0174	18 C	−0.26524	42 H	0.038769		
19 C	−0.0907	43 H	0.12228			19 C	0.106683	43 H	0.011003	67 H	−0.02139	19 C	0.093159	43 H	0.120604		
20 C	0.14225	44 H	−0.0034			20 C	−0.08115	44 H	0.024401	68 H	−0.01265	20 C	0.097984	44 H	0.007596		
21 O	−0.2633	45 H	0.02382			21 C	0.133992	45 H	0.127189	69 H	−0.00031	21 O	−0.29851	45 H	−0.01485		
22 O	−0.2669	46 H	−0.0183			22 C	0.043432	46 H	0.001705			22 O	−0.26741	46 H	−0.02284		
23 C	0.16286	47 H	−0.0082			23 O	−0.27654	47 H	−0.01308			23 C	0.164042	47 H	−0.03073		

Table 10 Energy (E in Hartree), dipole moment (μ in Debye), molecular volume (V in e bohr^{-3}) and the calculated quantum parameters (in eV and eV^{-1}) for **M1**, **M2** and **M3** inhibitors

	Neutral			Protonated		
	M1	**M2**	**M3**	**M1**	**M2**	**M3**
E_{Total} (N)	−1416.288	−1494.886	−1417.456	−1416.932	−1495.541	−1418.114
$E(N+1)$	−1416.329	−1494.926	−1417.497	−1416.984	−1495.597	−1418.170
$E(N-1)$	−1416.099	−1494.697	−1417.267	−1416.692	−1495.293	−1417.869
μ (D)	9.932	7.796	10.945	13.160	25.183	22.798
Volume	3462.222	3757.517	3574.804	3478.3639	3793.3213	3633.8774
E_{HOMO}	−5.042	−5.074	−5.273	−6.63	−6.78	−6.88
E_{LUMO}	−0.721	−0.448	−0.903	−1.22	−1.31	−1.31
ΔE_{gap}	4.321	4.625	4.3701	5.41	5.47	5.57
I_v	5.151	5.166	5.175	6.510	6.769	6.667
A_v	1.094	1.087	1.086	1.422	1.523	1.523
E_g	4.057	4.079	4.089	5.087	5.246	5.144
χ	2.882	2.761	3.088	3.925	4.045	4.095
η	2.161	2.313	2.185	2.705	2.735	2.785
S	0.463	0.432	0.458	0.370	0.366	0.359
Π	−2.8815	−2.761	−3.088	−3.925	−4.045	−4.095
ω	1.922	1.648	2.182	2.848	2.991	3.011
ε	0.520	0.607	0.458	0.351	0.334	0.332
ΔN	0.953	0.916	0.895	0.568	0.540	0.522
ΔE_1	−0.570	−0.297	−0.752	−1.069	−1.159	−1.159
ΔE_2	4.891	4.923	5.122	6.479	6.629	6.729
$E_{b\text{-}d}$	−0.540	−0.578	−0.546	−0.676	−0.684	−0.696

E_{Total}: electronic energy; $E(N+1)/E(N-1)$: energies of cation/anion; μ: dipole moment; volume: molecular volume; I_v: ionization potential; A_v: electron affinity; E_g: band gap; E_{HOMO}/E_{LUMO}: orbital energies; ΔE_{gap}: HOMO–LUMO gap; χ: electronegativity; $\Pi = -\chi$: chemical potential. η: hardness; S: softness; ω: electrophilicity index; ε: nucleophilicity index; ΔN: electron transfer fraction; ΔE_1, ΔE_2: interaction energies; $E_{b\text{-}d}$: back-donation energy.

Table 11 Comparison of ΔN (theoretical) and IE% (experimental)

Molecule	ΔN	IE%
M1	0.95	98.92
M2	0.92	98.22
M3	0.90	94.70

($R^2 \approx 0.046$ and 0.02, respectively), suggesting that these parameters alone cannot adequately describe the inhibition behavior. This observation highlights that corrosion inhibition is governed by a synergistic effect of multiple electronic factors rather than a single descriptor. Overall, the results confirm that the inhibition efficiency follows the order: **M1** > **M2** > **M3**.

Therefore, the present analysis demonstrates that ΔN serves as a reliable quantitative descriptor for correlating theoretical calculations with experimental inhibition efficiency.

3.5.2. Inhibitor-metal interaction type. In order to predict the type of interaction between the Fe and the inhibitors, and to propose a potential mechanism for the adsorption process, the energy gaps between the inhibitors and Fe-metal (ΔE_1 and ΔE_2) were estimated according to eqn (27) and (28).

$$\Delta E_1 = E_{LUMO}(\text{inhibitor}) - E_{LUMO}(\text{Fe}) \quad (27)$$

$$\Delta E_2 = E_{LUMO}(\text{Fe}) - E_{HOMO}(\text{inhibitor}) \quad (28)$$

where E_{HOMO} and E_{LUMO} of Fe are −7.9024 eV, and −0.151 eV, respectively.[130] ΔE_1 corresponds to the donated electrons from the d-orbitals of Fe surface, acting as a Lewis base, to the LUMO of the inhibitor as the Lewis acid. Meanwhile ΔE_2 indicates electrons donation from the HOMO of the inhibitor, acting as a Lewis base, to the vacant d-orbitals of Fe as Lewis acid. The ΔE_1 and ΔE_2 values are also calculated in Table 10, ΔE_1 is greater than ΔE_2 indicating that the compounds explored would preferentially behave as Lewis acids, with an affinity to donate electrons to the vacant d-orbitals of Fe.

3.5.3. Fukui functions and the local dual reactivity indices. Table S10 provides the calculated values of the local indices and their dual descriptors of the **M1**, **M2** and **M3** inhibitors, respectively. For the **M1**, the highest nucleophilic attack (f^+_k) are O24, N1 and C4, while the highest electrophilic attacks f^-_k) are C26, C27 and C29. In the case of the **M2** (neutral), the highest nucleophilic attack (f^+_k) are O26, N1 and C4, while the highest electrophilic attacks (f^-_k) are C28, C29, and C31. For the **M3**, the highest nucleophilic attack (f^+_k) are O24, N1 and C4, while the highest electrophilic attacks (f^-_k) are C26, C27 and C29. The estimated values of dual descriptors, which are shown in Table S10 of the SI, allow us to attain instantaneously the preferable sites for nucleophilic attacks (f_k^2, $\Delta\sigma_k$ and $\Delta\omega_k > 0$) and the preferable sites for electrophilic attacks (f_k^2, $\Delta\sigma_k$ and $\Delta\omega_k < 0$) over the system at point r.[131]

Fig. 17 displays the dual descriptors: f_k^2, $\Delta\sigma_k$ and $\Delta\omega_k$ of the neutral forms of **M1**, **M2** and **M3** compounds. As seen for the condensed Fukui functions and the local softness and philicity, the **M1**, **M2** and **M3** compounds have several active sites, and most of the active sites have a dual descriptor value lower than zero, besides some carbon atoms that have positive values. According to Fig. 17, it can be concluded that the most active sites that can interact with the iron surface in **M1**, **M2** and **M3** compounds are the oxygen and nitrogen atoms and some carbon atoms. However, in **M1**, **M2** and **M3** compounds, the

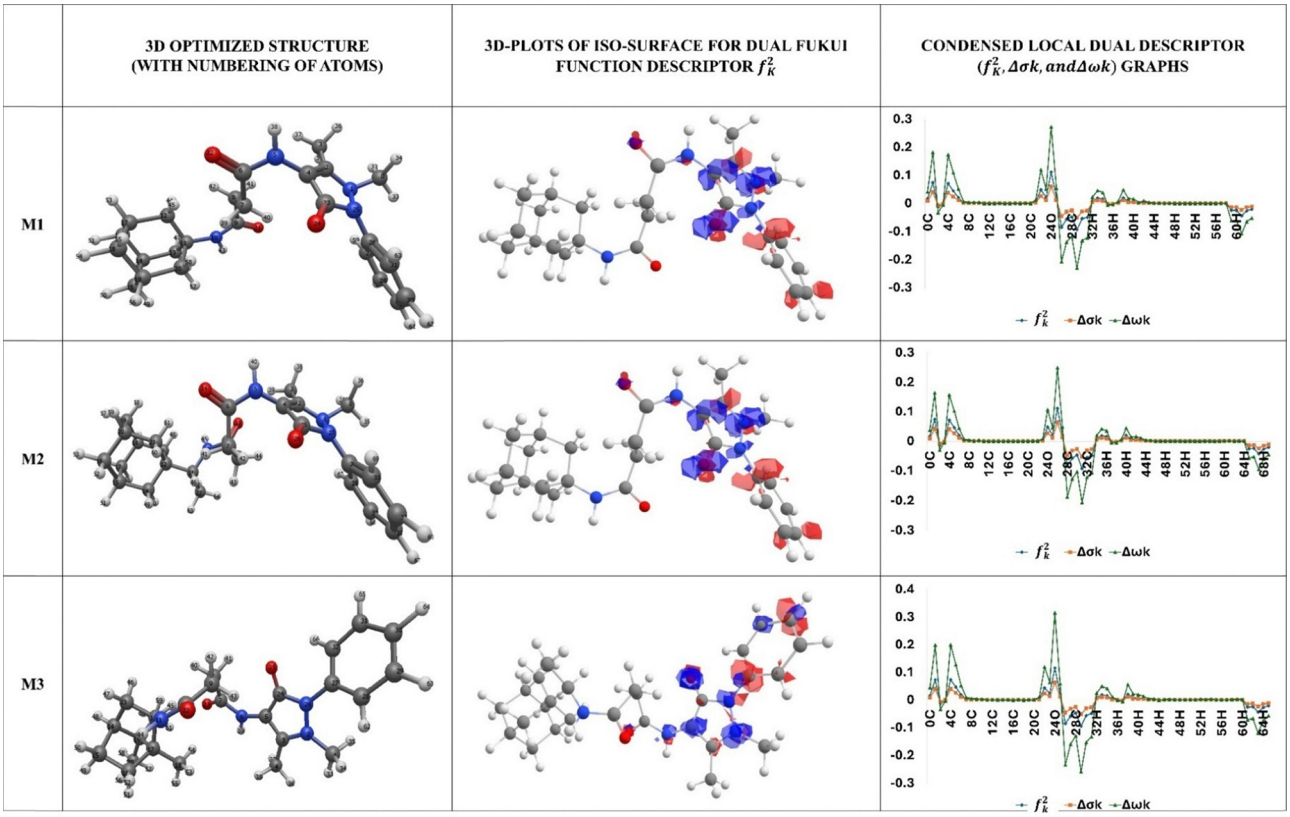

Fig. 17 (Left) 3D structure with atoms numbering of **M1**, **M2** and **M3**, (middle) 3D-plots of iso-surface for dual Fukui function descriptor (red lobes) correspond to positive region and the blue lobes correspond to the negative region, (right) the condensed local dual descriptor f_k^2, $\Delta\sigma_k$, and $\Delta\omega_k$ based on Fukui functions.

different carbon atom of benzene ring is the site to accept electron of the Fe surface to form back-bonding interactions. These results are consistent with the results obtained *via* the HOMO, LUMO evaluations.

3.6. Corrosion inhibition mechanism

The organic inhibitor inhibits metal corrosion through an adsorption process.[132] In the adsorption process, the water molecules and other corrosion species on the metal surface are replaced by the inhibitor molecules. The state of organic molecules and the metal surface charge influence the adsorption process in the acidic environment.[133] The mild steel in HCl carries a net positive charge, which causes the adsorption of chloride ions on the surface. Moreover, excess electrons are generated which facilitates the adsorption of the cationic species on the surface of mild steel. In the present study, the **M1**, **M2**, **M3** have many sites available for interaction with mild steel surface. The interaction with mild steel surface through the amide linkage from antipyrine ring side and amide linkage from the adamantyl group side can be possible. The DFT studies show that the amide linkage from the antipyrine side, nitrogen of antipyrine ring are mainly involved to form interactions with steel surface. Whereas, in HCl solution, the **M1**, **M2**, and **M3** may be protonated to from the electrostatic interaction with the chloride ions on the surface of mild steel leading to the physiosorption of the inhibitor molecules. The proposed mechanism is shown in Fig. 18. The **M1** show the donation of electrons through the O, and N sites from the amide group attached to the antipyrine ring and nitrogen and oxygen from the antipyrine ring. Moreover, the oxygen of amide attached to the adamantyl group also involved in inhibiting the surface. The bonding interaction of the **M1** with the mild steel surface is though the vacant d orbitals of mild steel.

4. Conclusion

In conclusion, the study demonstrates the effectiveness of newly synthesized compounds **M1**, **M2**, and **M3** as corrosion inhibitors for mild steel in an acidic environment by using both experimental and theoretical methods. The key findings and observations are summarized as follows:

1. The study shows that the **M1**, **M2** and **M3** are effective corrosion inhibitors for mild steel in acidic solution. It was observed that the corrosion rate decreases and IE% increases both by increasing the immersion time and concentration. Elevated temperature decreases the IE% and increases the corrosion rate.

2. Different thermodynamic parameters like activation energy (E_a), Enthalpy changes ΔH, Entropy change ΔS and Gibb's free energy change ΔG elaborates the adsorption of inhibitors on the surface of mild steel to mitigate the corrosion.

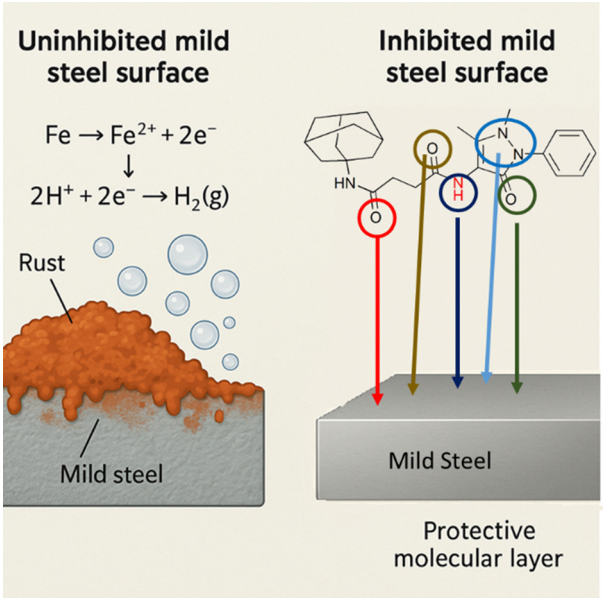

Fig. 18 Proposed mechanism of inhibition of the mild steel surfaces using **M1**.

This adsorption creates a protective layer on the mild steel that acts as a barrier to prevent corrosion entities from attacking on the metals. These thermodynamic parameters collectively indicated that adsorption procedure of these inhibitors is the mixture of physisorption and chemisorption depends of various conditions like temperature.

3. Electrochemical analysis, both PDP and EIS methods were used to assess the anticorrosion properties of the inhibitors. Various parameters calculated from these analyses provide the valuable information about the kinetics of corrosion process which reveals the extraordinary inhibitory properties of the inhibitors.

4. The literature study shows that these inhibitors comprise of nontoxic, ecofriendly and readily available structural fragments. The reagents and instrumentations need for the synthesis of these inhibitors are very cheap which make it more economic.

5. The quantum chemical and DFT measurements support the experimental data and proves the exceptional inhibitory efficiency of inhibitors.

In summary, these compounds show increased inhibition efficiency with higher concentrations and longer exposure times. The anti-corrosion potential of the compounds decreases at higher temperatures. Among these inhibitors (**M1**–**M3**), **M1** exhibits the highest anticorrosion potential due to the lower steric hindrance on the adamantyl group in its structure. The research combines experimental and theoretical approaches, providing comprehensive insights into the inhibition mechanisms and highlighting the potential of these compounds for applications in corrosion protection.

Conflicts of interest

The authors declare no conflict of interests.

Data availability

The supporting data has been provided as part of the supplementary information (SI). it contains following files SI-1: it contains the characterization data NMR, FTIR, MS *etc.* and Table S11. SI-2: it contains Tables S1–S9 and S10. See DOI: https://doi.org/10.1039/d6ma00114a.

Acknowledgements

This research work is supported by the Ministry of Higher Education (MOHE) under the 2023 Translational Research Program for the Energy Sustainability Focus Area (Project ID: MMUE/240001), the 2024 ASEAN IVO (Project ID: 2024-02), and Multimedia University, Malaysia. Adil Afaq thanks the Higher Education Commission of Pakistan for IRSIP funding. Md. Akhtaruzzam acknowledges the Deanship of Graduate Studies and Scientific Research at the Islamic University of Madinah for the research support Program.

References

1 C. Verma, E. E. Ebenso, M. Quraishi and C. M. Hussain, *Mater. Adv.*, 2021, **2**, 3806–3850.
2 Q. Zhang, R. Zhang, L. Guo and I. B. Obot, *Anti-Corrosive Nanomaterials*, CRC Press, 2023, pp. 323–330.
3 G. Srinivasan, A. Manickam, S. Sivakumar, J. Murugan, S. Elangomannan and S. Mohan, *J. Mater. Sci.: Mater. Eng.*, 2025, **20**, 76.
4 M. Quraishi, D. S. Chauhan and F. A. Ansari, *J. Mol. Liq.*, 2021, **329**, 115514.
5 M. Sharma, N. Tellili, I. Kacem and T. Rouissi, *Appl. Sci.*, 2024, **14**, 5081.
6 E. E. Ebenso, C. Verma, L. O. Olasunkanmi, E. D. Akpan, D. K. Verma, H. Lgaz, L. Guo, S. Kaya and M. A. Quraishi, *Phys. Chem. Chem. Phys.*, 2021, **23**, 19987–20027.
7 T. Bayrak and M. Olu, *J. Agricultural Prod.*, 2025, **6**, 157–166.
8 A. O. Alaoui, W. Elfalleh, B. Hammouti, A. Titi, M. Messali, S. Kaya, B. E. IBrahimi and F. El-Hajjaji, *RSC Adv.*, 2025, **15**, 12645–12652.
9 H. Lgaz, A. Chaouiki, R. Lamouri, R. Salghi and H.-S. Lee, *Sustainable Corrosion Inhibitors I: Fundamentals, Methodologies, and Industrial Applications*, ACS Publications, 2021, pp. 87–109.
10 A. A. Al-Amiery, W. N. R. W. Isahak and W. K. Al-Azzawi, *Lubricants*, 2023, **11**, 174.
11 C. I. Ekeocha, I. N. Uzochukwu, I. B. Onyeachu, I.-I. N. Etim and E. E. Oguzie, *Struct. Chem.*, 2025, **36**, 363–379.
12 A. Narayanswamy, D. Ramakrishna, P. R. Shekar, S. Rajendrachari and R. Sudhakar, *ACS Omega*, 2024, **9**, 13262–13273.
13 A. Upadhyay, A. K. Purohit, G. Mahakur, S. Dash and P. K. Kar, *J. Mol. Liq.*, 2021, **333**, 115960.
14 R. Çakmak, B. Dağ and F. Yaşar, Chair of the Conference, 2013, p. 106.
15 N. Ranjitha, G. Krishnamurthy, H. B. Naik, M. Pari, L. Afroz, K. Sumadevi and M. Manjunatha, *Inorg. Chim. Acta*, 2022, **543**, 121191.

16 A. Erbaş, S. Dikim, F. Arslan, O. C. Bodur, S. Arslan, F. Özdemir and N. Sarı, *Bioinorg. Chem. Appl.*, 2025, **2025**, 2786064.
17 C. J. Dhanaraj, *Appl. Biochem. Biotechnol.*, 2025, **197**, 3048–3079.
18 F. Afshari, E. R. Ghomi, M. Dinari and S. Ramakrishna, *ChemistrySelect*, 2023, **8**, e202203231.
19 A. Narayanswamy, D. Ramakrishna and R. Sudhakar, *Chem. Pap.*, 2025, **79**, 333–352.
20 R. Liu, Y. Wang, Y. Yang, L. Shen, B. Zhang, Z. Dong, C. Gao and B. Xing, *Environ. Pollut.*, 2023, **317**, 120818.
21 P. D. Desai, C. B. Pawar, M. S. Avhad and A. P. More, *Vietnam J. Chem.*, 2023, **61**, 15–42.
22 E. A. Aydinsoy, Z. Z. Aghamaliyev, D. B. Aghamaliyeva and V. B. Abbasov, *Processes Petrochem. Oil Refin.*, 2024, **25**, 793–843.
23 A. Dehghani, E. Berdimurodov, C. Verma, D. K. Verma, K. Berdimuradov, M. Quraishi and N. Aliev, *Chem. Pap.*, 2024, **78**, 1367–1397.
24 A. P. Singh Raman, A. A. Muhammad, H. Singh, T. Singh, Z. Mkhize, P. Jain, S. K. Singh, I. Bahadur and P. Singh, *ACS Omega*, 2022, **7**, 47471–47489.
25 K. Gongsun, Z. Gang, X. Gao, J. Qiu, K. Feng, C. Chen, C. Bu, X. Li and H. Ma, *Chem. Eng. J.*, 2025, 171176.
26 E. Ebenso, U. Ekpe, B. Ita, O. Offiong and U. Ibok, *Mater. Chem. Phys.*, 1999, **60**, 79–90.
27 X. Yan, Z. Yang, R. Wang, W. Xiang, Z. Yang, C. Sun, Q. Yu, M. Cai and B. Yu, *Tribol. Int.*, 2023, **177**, 107925.
28 G. Gómez-Sánchez, V. Díaz-Jiménez, P. Arellanes-Lozada, I. V. Lijanova, J. Arriola-Morales, M. Castillo-Morales, N. V. Likhanova and O. Olivares-Xometl, *Molecules*, 2025, **30**, 3994.
29 D. M. Mamad, H. H. Rasul, A. H. Awla and R. A. Omer, *Dokl. Phys. Chem.*, 2023, **511**, 125–133.
30 M. Liu, J. Liu, Z. Zeng, X. Wang, J. Jia, X. Gu and Z. Zheng, *Sep. Purif. Technol.*, 2022, **300**, 121929.
31 M. A. M. Alwi, M. N. Ahmad, B. M. Piah, H. Pauzi and E. Normaya, *J. Mol. Struct.*, 2025, **1345**, 142961.
32 Y. Yetri, G. Gunawarman, R. Rakiman, A. Y. Rivai and I. Nur, *Solid State Phenom.*, 2024, **357**, 69–82.
33 L. J. Arachchige, C. Li and F. Wang, *ChemRxiv*, 2024.
34 P. Strazzolini, N. Misuri and P. Polese, *Tetrahedron Lett.*, 2005, **46**, 2075–2078.
35 S. Cunha, S. M. Oliveira, M. T. Rodrigues Jr, R. M. Bastos, J. Ferrari, C. M. de Oliveira, L. Kato, H. B. Napolitano, I. Vencato and C. Lariucci, *J. Mol. Struct.*, 2005, **752**, 32–39.
36 J. Porter, A. R. Noble, N. Signoret, M. A. Fascione and G. J. Miller, *ACS Omega*, 2024, **9**, 31703–31713.
37 H. S. Aljibori, A. Alamiery, T. S. Gaaz and W. K. Al-Azzawi, *Carbon Neutralization*, 2024, **3**, 74–93.
38 A. Nace, *ASTM Int.*, 2012, **100**, 19428–12959.
39 S. A. Umoren, M. M. Solomon, I. B. Obot and R. K. Suleiman, *Sustainability*, 2021, **13**, 5569.
40 B. El Ibrahimi and E. Berdimurodov, *Electrochemical and analytical techniques for sustainable corrosion monitoring*, Elsevier, 2023, pp. 81–90.
41 E. C. Freire, A. T. García, C. Redroban, J. C. Vega and F. G. Rodriguez, *ESPOCH Congresses: Ecuadorian J. STEAM*, 2024, 179–192.
42 M. Pavithra, T. Venkatesha, K. Vathsala and K. Nayana, *Corros. Sci.*, 2010, **52**, 3811–3819.
43 M. Pavithra, T. Venkatesha, M. Punith Kumar and K. Manjunatha, *Res. Chem. Intermed.*, 2015, **41**, 7163–7177.
44 A. Ech-chebab, K. Dahmani, R. Hsissou, O. El Khouja, D. K. Verma, E. Berdimurodov, Ş. Erdoğan, B. Tüzün, R. Lachhab and A. Ejbouh, *J. Mol. Struct.*, 2023, **1284**, 135441.
45 Z. El-Kiri, A. Hmada, R. Sayed, K. Dakhsi, A. Larioui, F. Benhiba, R. Hsissou, N. Dkhireche, M. Galai and M. EbnTouhami, *J. Mol. Struct.*, 2023, **1294**, 136466.
46 D. Ramakrishna, B. R. Bhat and R. Karvembu, *Catal. Commun.*, 2010, **11**, 498–501.
47 A. Nandiyanto, A. Wiryani, A. Rusli, A. Purnamasari, A. Abdullah, I. Widiaty and R. Hurriyati, *IOP Conf. Ser.:-Mater. Sci. Eng.*, 2017, **180**, 012136.
48 P. Gunasekaran, Y. Velmurugan, D. S. Arputharaj, J. K. Savaridasson, M. Hemamalini and R. Venkatachalam, *Front. Chem.*, 2023, **11**, 1096177.
49 F. Neese, *Wiley Interdiscip. Rev.: Comput. Mol. Sci.*, 2018, **8**, e1327.
50 M. Elkabous, M. Ouachekradi and Y. Karzazi, *Chem. Phys. Mater.*, 2025, **5**, 71–82.
51 I. Sandler, *Predicting and understanding binding affinities of synthetic anion receptors*, University of New South Wales, Australia, 2023.
52 B. Mennucci, J. Tomasi, R. Cammi, J. R. Cheeseman, M. J. Frisch, F. J. Devlin, S. Gabriel and P. J. Stephens, *J. Phys. Chem. A*, 2002, **106**, 6102–6113.
53 R. Hsissou, F. Benhiba, M. El Aboubi, S. Abbout, Z. Benzekri, Z. Safi, M. Rafik, H. Bahaj, M. Kaba and M. Galai, *Chem. Phys. Lett.*, 2022, **806**, 139995.
54 J. Simons, *J. Phys. Chem. A*, 2024, **128**, 8436–8445.
55 J. Zhao, J. Guo, C. Wang and K. Wang, *Eur. Phys. J. Plus*, 2024, **139**, 1033.
56 R. Haldhar, D. Prasad and A. Saxena, *J. Environ. Chem. Eng.*, 2018, **6**, 5230–5238.
57 S. Zamindar, S. Mandal, M. Murmu and P. Banerjee, *Mater. Adv.*, 2024, **5**, 4563–4600.
58 S. K. Saha and P. Banerjee, *Mater. Chem. Front.*, 2018, **2**, 1674–1691.
59 F. Philippi and T. Welton, *Phys. Chem. Chem. Phys.*, 2021, **23**, 6993–7021.
60 S. Deng, X. Li and X. Xie, *Corros. Sci.*, 2014, **80**, 276–289.
61 T. Koopmans, *Physica*, 1934, **1**, 104–113.
62 T. Peme, L. O. Olasunkanmi, I. Bahadur, A. S. Adekunle, M. M. Kabanda and E. E. Ebenso, *Molecules*, 2015, **20**, 16004–16029.
63 B. Gómez, N. V. Likhanova, M. A. Domínguez-Aguilar, R. Martínez-Palou, A. Vela and J. L. Gazquez, *J. Phys. Chem. B*, 2006, **110**, 8928–8934.
64 M. Damej, A. Molhi, H. Lgaz, R. Hsissou, J. Aslam, M. Benmessaoud, N. Rezki, H. S. Lee and D. Lee, *J. Mol. Struct.*, 2023, **1273**, 134232.
65 A. El Magri, R. Hsissou, A. Hmada, A. Berisha, N. Dkhireche and S. Vaudreuil, *J. Mol. Liq.*, 2023, **387**, 122690.

66 M. Azogagh, A. El Magri, R. Hsissou, R. Lachhab, K. P. Katin, E. Berdimurodov, M. Galai, S. Hegazi and M. Rafik, *J. Mol. Liq.*, 2024, **416**, 126459.
67 S. R. Odilov, DATE FRUIT UTILIZING, POMACE AS A CORROSION GREEN INHIBITOR FOR NON FERROUS, ALLOYS, 2025.
68 O. Safdarzadeh, A. Farahi, A. Binder, H. Sezen and J. P. Hofmann, *Lubricants*, 2024, **12**, 148.
69 S. A. Asher, A. Ianoul, G. Mix, M. N. Boyden, A. Karnoup, M. Diem and R. Schweitzer-Stenner, *J. Am. Chem. Soc.*, 2001, **123**, 11775–11781.
70 R. Thurston, V. Zantop, K. S. Park, H. Maid, A. Seitz and M. R. Heinrich, *Org. Lett.*, 2022, **24**, 3488–3492.
71 K. Fu, Z. Yang, Z. Liu, X. Mai, Y. Cai, X. Li, W. Feng, L. Yuan and B. Gong, *J. Am. Chem. Soc.*, 2026, **148**(8), 8285–8297.
72 Y. Meng, X. Yang, S. Cao, X. Pan, Y. Yang, H. Zhang, X. Sui and T. Liu, *Ind. Crops Prod.*, 2025, **228**, 120905.
73 S. K. Saha, M. Murmu, N. C. Murmu and P. Banerjee, *J. Mol. Liq.*, 2022, **364**, 120033.
74 X. Zhang, Y. Zhang, Y. Su, X. Wang and R. Lv, *ACS Omega*, 2022, **7**, 32208–32224.
75 C.-A. Xu, X. Li, Z. Tong, Z. Chu, H. Fang, Y. Hu, X. Chen and Z. Yang, *Chem. Eng. J.*, 2024, **483**, 149316.
76 N. A. Odewunmi, M. A. Mazumder and S. A. Ali, *J. Mol. Liq.*, 2022, **360**, 119431.
77 N. Wazzan, I. Obot and T. M. Fagieh, *Desalination*, 2022, **527**, 115551.
78 C. Sangeetha, C. Chinnakani, P. DeepaRani and S. Selvaraj, *J. Adv. Sci. Res.*, 2020, **11**, 180–186.
79 M. Abbass, K. Raheef, I. Aziz, M. Hanoon, A. Mustafa, W. Al-Azzawi, A. Al-Amiery and A. Kadhum, *Prog. Color, Color. Coat.*, 2024, **17**, 1–10.
80 A. A. Farag, H. E. Abdallah, E. A. Badr, E. A. Mohamed, A. I. Ali and A. El-Etre, *J. Mol. Liq.*, 2021, **341**, 117348.
81 A. Kokalj, *Corros. Sci.*, 2021, **193**, 109650.
82 A. Soni, P. Sharma, R. D. Monika and A. Goswami, *Port. Electrochim. Acta*, 2017, **35**, 117–126.
83 C. G. Vaszilcsin, M. V. Putz, A. Kellenberger and M. L. Dan, *J. Mol. Struct.*, 2023, **1286**, 135643.
84 S. Yang, A. Chen, Z. Tang, Z. Wu, P. Li, Y. Wang, X. Wang, X. Jin, S. Bai and C. Zhi, *Energy Environ. Sci.*, 2024, **17**, 1095–1106.
85 B. Kabylbekova, N. Vysotskaya, A. Anarbaev, R. Spabekova, K. Kurbanbekov, G. Kaldybekova and Z. Khussanov, *ChemEngineering*, 2025, **9**, 133.
86 S. Budhathoki, N. Chaudhary, B. Guragain, D. Baral, J. Adhikari and N. K. Chaudhary, *Heliyon*, 2024, 10.
87 K. Ivanković, M. Kern and M. Rožman, *J. Hazard. Mater.*, 2021, **414**, 125554.
88 H. J. Kreuzer and Z. W. Gortel, *Physisorption kinetics*, Springer Science & Business Media, 2012.
89 O. Diwald and M. Hartmann, *Metal Oxide Nanoparticles: Formation, Functional Properties, and Interfaces*, 2021, **2**, 593–636.
90 A. Toghan, H. Gadow, A. Fawzy, H. Alhussain and H. Salah, *Metals*, 2023, **13**, 1565.
91 X. Du, Y. Cheng, Z. Liu, H. Yin, T. Wu, L. Huo and C. Shu, *Fuel*, 2021, **283**, 118886.
92 K. A. Othman, W. M. Hamad and R. A. Omer, *Corr. Rev.*, 2025, **43**, 335–359.
93 B. J. Riley, J. R. Turner, J. McFarlane, S. Chong, K. Carlson and J. Matyáš, *Mater. Adv.*, 2024, **5**, 9515–9547.
94 A. Barrahi, M. El Faydy, F. Benhiba, H. S. Kusuma, D. Bazanov, N. A. Lozinskaya, I. Warad, B. Dikici and A. Zarrouk, *Indian Chem. Eng.*, 2025, 1–21.
95 R. Hsissou, A. El Magri, E. Ech-chihbi, A. Hmada, I. Saber, A. Berisha, N. Dkhireche, D. Ouzebla, M. Rbaa and F. Benhiba, *Can. Metall. Q.*, 2025, **64**, 1333–1350.
96 G. Laadam, N. Timoudan, A. Dahmani, S. Daoui, A. Thakur, H. A. Abuelizz, M. E. Faydy, F. Benhiba, I. Warad and N. Benchat, *Can. Metall. Q.*, 2025, 1–21.
97 M. El Faydy, A. Barrahi, N. Timoudan, I. Warad, Z. Safi, N. Wazzan, G. Kaichouh, F. Benhiba, A. Dafali and B. Lakhrissi, *Can. Metall. Q.*, 2025, 1–23.
98 A. Kadhim, N. Betti, A. Al-Adili, L. Shaker and A. Al-Amiery, *Int. J. Corros. Scale Inhib.*, 2022, **11**, 43–63.
99 M. Zhang, F. Xu, D. Lin, J. Peng, Y. Zhu and H. Wang, *Chem. Eng. J.*, 2022, **446**, 137078.
100 S. Varvara, G. Caniglia, J. Izquierdo, R. Bostan, L. Găină, O. Bobis and R. M. Souto, *Corros. Sci.*, 2020, **165**, 108381.
101 J. Pan, D. Thierry and C. Leygraf, *Electrochim. Acta*, 1996, **41**, 1143–1153.
102 R. S. Raman, A. Sanjid, P. C. Banerjee, A. K. Arya, R. Parmar, M. Amati and L. Gregoratti, *Small*, 2024, **20**, 2302498.
103 S. Li, S. Hu, F. Wang, F. Zhang, W. Hu, X. Zhao, Y. Tang and Y. Zuo, *Electrochim. Acta*, 2024, **480**, 143887.
104 Z. Chen, Z. Guo and A. A. Fadhil, *J. Build. Eng.*, 2025, 113815.
105 J. Wu, *Chem. Rev.*, 2022, **122**, 10821–10859.
106 I. B. Onyeachu, I. B. Obot and A. Y. Adesina, *Corros. Sci.*, 2020, **168**, 108589.
107 M. C. Luna, T. Le Manh, R. C. Sierra, J. M. Flores, L. L. Rojas and E. A. Estrada, *J. Mol. Liq.*, 2019, **289**, 111106.
108 M. Salman, K. Ansari, V. Srivastava, D. S. Chauhan, J. Haque and M. Quraishi, *J. Mol. Liq.*, 2021, **322**, 114825.
109 K. Bijapur, V. Molahalli, A. Shetty, A. Toghan, P. De Padova and G. Hegde, *Appl. Sci.*, 2023, **13**, 10107.
110 A. Tazi, O. Dagdag, A. El Amri, M. Rafik, M. Azogagh, H. Haidara, H. Kim, A. El Bachiri, A. Berisha and E. Berdimurodov, *J. Mater. Sci.*, 2025, **60**, 16952–16972.
111 F. Malaret and X.-S. Yang, *Exp. Results*, 2022, **3**, e13.
112 S. Mourdikoudis and X. Dominguez-Benetton, *Chemistry-Methods*, 2025, **5**, e202400046.
113 K. Govindaraju, D. Gopi and L. Kavitha, *J. Appl. Electrochem.*, 2009, **39**, 2345–2352.
114 A. Eldesoky, M. Ghoneim, M. Diab, A. El-Bindary, A. El-Sonbati and M. Abd El-Kader, *J. Mater. Environ. Sci.*, 2015, **6**, 3066–3085.
115 N. C. Okey, N. L. Obasi, P. M. Ejikeme, D. T. Ndinteh, P. Ramasami, E.-S. M. Sherif, E. D. Akpan and E. E. Ebenso, *J. Mol. Liq.*, 2020, **315**, 113773.
116 K. F. Khaled and N. Hackerman, *Mater. Chem. Phys.*, 2003, **82**, 949–960.

117 M. Bahrami, S. Hosseini and P. Pilvar, *Corros. Sci.*, 2010, **52**, 2793–2803.
118 N. Ashwini, D. Ramakrishna and S. Ranganatha, *Results Surf. Interfaces*, 2024, **15**, 100209.
119 A. Dementjev, A. De Graaf, M. Van de Sanden, K. Maslakov, A. Naumkin and A. Serov, *Diamond Relat. Mater.*, 2000, **9**, 1904–1907.
120 P. Mourya, P. Singh, A. Tewari, R. Rastogi and M. Singh, *Corros. Sci.*, 2015, **95**, 71–87.
121 O. Olivares-Xometl, N. Likhanova, M. Domínguez-Aguilar, J. Hallen, L. Zamudio and E. Arce, *Appl. Surf. Sci.*, 2006, **252**, 2139–2152.
122 A. Singh, K. R. Ansari, M. A. Quraishi and H. Lgaz, *Materials*, 2018, **12**, 17.
123 S. Ralkhal, T. Shahrabi, B. Ramezanzadeh and G. Bahlakeh, *Appl. Surf. Sci.*, 2019, **464**, 178–194.
124 I. Obot, D. Macdonald and Z. Gasem, *Corros. Sci.*, 2015, **99**, 1–30.
125 B. S. Mahdi, M. K. Abbass, M. K. Mohsin, W. K. Al-Azzawi, M. M. Hanoon, M. H. H. Al-Kaabi, L. M. Shaker, A. A. Al-Amiery, W. N. R. W. Isahak and A. A. H. Kadhum, *Molecules*, 2022, **27**, 4857.
126 B. C. Sahu, *Introduction to corrosion-Basics and advances*, IntechOpen, 2023.
127 I. Obot, A. Madhankumar, S. Umoren and Z. Gasem, *J. Adhes. Sci. Technol.*, 2015, **29**, 2130–2152.
128 C. Verma, E. E. Ebenso, I. Bahadur and M. Quraishi, *J. Mol. Liq.*, 2018, **266**, 577–590.
129 R. M. Issa, M. K. Awad and F. M. Atlam, *Appl. Surf. Sci.*, 2008, **255**, 2433–2441.
130 J. I. Martínez-Araya, *J. Math. Chem.*, 2015, **53**, 451–465.
131 A. H. Moustafa, H. H. Abdel-Rahman, A. Barakat, H. A. Mohamed and A. S. El-Kholany, *ACS Omega*, 2024, **9**, 16469–16485.
132 S. A. Umoren, M. M. Solomon, S. A. Ali and H. D. Dafalla, *Mater. Sci. Eng., C*, 2019, **100**, 897–914.
133 H. M. Abd El-Lateef, *Appl. Surf. Sci.*, 2020, **501**, 144237.